


Article

LA-ICP-MS U-Th-Pb Dating and Trace Element Geochemistry of Allanite: Implications on the Different Skarn Metallogenesis between the Giant Beiya Au and Machangqing Cu-Mo-(Au) Deposits in Yunnan, SW China

Yu Fu ^{1,2}, Xiaoming Sun ^{1,2,3,*}, Dengfeng Li ^{1,2}, Hai Lin ^{2,3} and Chunkit Lai ^{4,5} 

¹ School of Marine Sciences, Sun Yat-sen University, Guangzhou 510006, China; fuyu26@mail.sysu.edu.cn (Y.F.); lidf3@mail.sysu.edu.cn (D.L.)

² Guangdong Provincial Key Laboratory of Marine Resources and Coastal Engineering, Guangzhou 510275, China; linhai7@mail2.sysu.edu.cn

³ School of Earth Science and Engineering, Sun Yat-sen University, Guangzhou 510275, China

⁴ Faculty of Science, University of Brunei Darussalam, Gadong BE1410, Brunei Darussalam; chunkitl@utas.edu.au

⁵ ARC Centre for Excellence in Ore Deposits (CODES), University of Tasmania, Hobart 7001, Australia

* Correspondence: eessxm@mail.sysu.edu.cn; Tel.: +86-20-8411-0968

Received: 30 October 2017; Accepted: 15 December 2017; Published: 19 December 2017

Abstract: The giant Beiya Au skarn deposit and Machangqing porphyry Cu-Mo-(Au) deposit are located in the middle part of the Jinshajiang–Ailaoshan alkaline porphyry metallogenic belt. The Beiya deposit is the largest Au skarn deposit in China, whilst the Machangqing deposit comprises a well-developed porphyry-skarn-epithermal Cu-Mo-(Au) mineral system. In this paper, we present new allanite U-Th-Pb ages and trace element geochemical data from the two deposits and discuss their respective skarn metallogenesis. Based on the mineral assemblage, texture and Th/U ratio, the allanite from the Beiya and Machangqing deposits are likely hydrothermal rather than magmatic. Laser ablation-inductively coupled plasma-mass spectrometry (LA-ICP-MS) allanite U-Th-Pb dating has yielded Th-Pb isochron ages of 33.4 ± 4.6 Ma (MSWD = 0.22) (Beiya) and 35.4 ± 9.8 Ma (MSWD = 0.26) (Machangqing), representing the retrograde alteration and magnetite skarn mineralization age of the two deposits. The Beiya and Machangqing alkali porphyry-related mineralization are synchronous and genetically linked to the magmatic hydrothermal activities of the Himalayan orogenic event. Major and trace element compositions reveal that the Beiya allanite has higher $\text{Fe}^{3+}/(\text{Fe}^{3+} + \text{Fe}^{2+})$ ratios, U content and Th content than the Machangqing allanite, which indicate a higher oxygen fugacity and F content for the ore-forming fluids at Beiya. Such differences in the ore-forming fluids may have contributed to the different metallogenic scales and metal types in the Beiya and Machangqing deposit.

Keywords: allanite; U-Th-Pb dating; trace elements; giant Beiya Au skarn deposit; Machangqing porphyry Cu-Mo deposit; Sanjiang region (SW China)

1. Introduction

Allanite $((\text{Ca}, \text{REE}, \text{Th})_2(\text{Fe}, \text{Al})_3\text{Si}_3\text{O}_{12}(\text{OH}))$ is a rare earth element (REE)-rich epidote-group mineral, and is commonly found in many magmatic/metamorphic rocks and hydrothermal mineral systems, especially in skarn and IOCG (iron-oxide copper gold). Allanite typically contains high U, Th and REE concentrations, which can be used for age dating and tracing various magmatic, metamorphic and ore-forming processes [1]. Allanite is a highly resistate mineral and has high closure

temperature, rendering it a useful age dating material [2]. Allanite could crystallize in a wider range of metamorphic P-T conditions than zircon and monazite [3], and its common larger size enables the preservation of internal chemical and isotopic zoning [4]. Allanite has been increasingly used to date metamorphic events [5–10]. Compared to igneous and metamorphic petrogenetic research, in-situ laser ablation-inductively coupled plasma-mass spectrometry (LA-ICP-MS) allanite dating and trace element analyses have not been widely used to investigate hydrothermal metallogenesis. In recent years, there are attempts to directly constrain skarn mineralization age using allanite U-Th-Pb dating [11,12], and to use allanite as tracer of the multiple hydrothermal fluid phases [13]. Although allanite commonly contains higher initial common Pb than zircon (which makes it harder to yield a concordant age) [4,14], allanite U-Th-Pb can still yield geological meaningful ages given that appropriate common Pb correction methods are adopted [4,14–18].

The giant Beiya Au-polymetallic skarn deposit is situated in the middle part of the Jinshajiang–Ailaoshan alkaline porphyry metallogenic belt. The deposit is the largest Au skarn deposit in China, with estimated ore reserves of 130.8 million tonnes (Mt) Au @ 2.47 g/t, 170 Mt Fe @ 33.3 wt %, 125 Mt Cu @ 0.52 wt %, along with considerable amounts of Pb, Zn and Ag [19,20]. The Jinshajiang–Ailaoshan alkaline porphyry metallogenic belt is an important Cu-Au province in SW China, and contains a large number of deposits that are spacetime associated with the Cenozoic (Himalayan) alkaline magmatism [21–24]. Ore deposit geology, ore fluid composition and metallogenetic studies of the Beiya Au mineralization all suggest that the Beiya deposit resembles typical porphyry-related Au skarn deposits worldwide [25–29].

The Machangqing porphyry Cu-Mo-(Au) deposit near Beiya is also located in the middle part of the Jinshajiang–Ailaoshan metallogenic belt, and the mineral system also contains porphyry-related skarn and epithermal Cu-(Au) mineralization [23,30–32]. The two deposits likely share common post-collisional metallogenetic settings and alkali porphyry-related mineralization style, but they differ greatly in terms of the ore deposit size and types of metals. Previous age dating studies have focused on the Machangqing intrusive complex and the molybdenite of the porphyry mineralization [23,32–36], whereas age constraints on the skarn mineralization are lacking.

Direct and precise dating of the skarn mineralization is pivotal to reveal the hydrothermal ore-forming processes of the Beiya and Machangqing deposits, to establish any genetic link with the regional alkaline magmatism, and to correlate the skarn mineralization in various parts of the Jinshajiang–Ailaoshan metallogenic belt [37]. In this study, we present new U-Th-Pb age and trace element data on the hydrothermal allanite from the Beiya and Machangqing deposits. Our new data are integrated with published data to discuss the ore-forming environment and magmatic-hydrothermal evolution of these two porphyry-related mineral systems.

2. Geological Background

2.1. Regional Geology

The Jinshajiang–Ailaoshan alkali porphyry metallogenic belt is located in the Sanjiang Tethyan domain in SW China (Figure 1) [21,38], and is bounded by the South China Block to the east along the Jinshajiang–Ailaoshan suture zone [39,40]. Many large porphyry and skarn deposits are associated with this belt, which makes it one of the most important metallogenetic belts in China. The Jinshajiang–Ailaoshan alkali porphyry metallogenic belt includes two subbelts: the Yulong porphyry subbelt in the north and the Ailaoshan-Red River porphyry subbelt in the south [28].

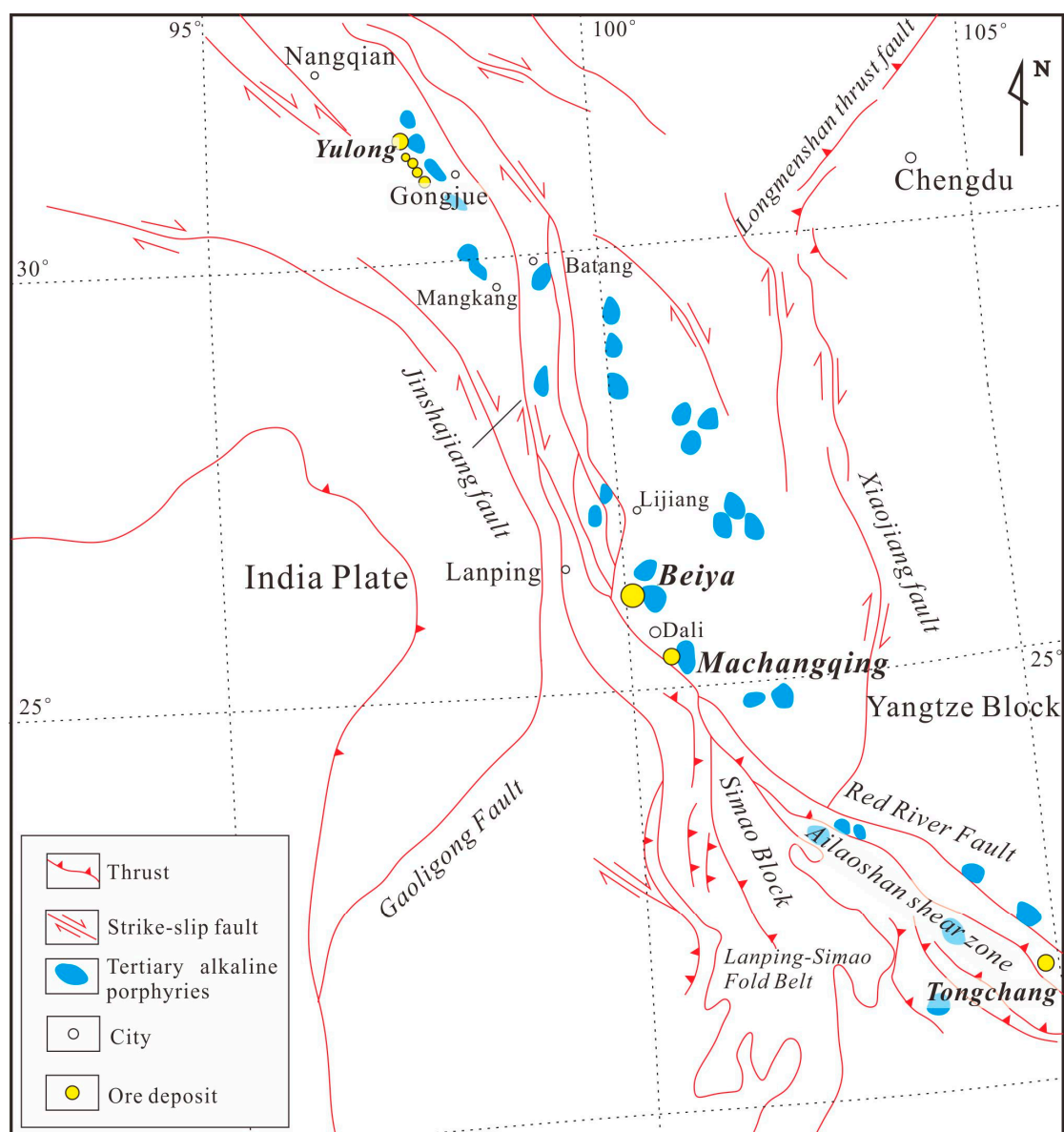


Figure 1. Tectonic map of the Beiya and Machangqing deposit. Modified after [41,42].

The Beiya and Machangqing deposits are located in the eastern side of the Jinshajiang suture (Figure 1). Major igneous rocks emplaced in/around the Beiya ore district include the Late Permian Emeishan continental flood basalt and the Cenozoic alkaline porphyries. The Emeishan flood basalt is exposed in the southeastern part of the mining area. The regionally-widespread Cenozoic alkaline porphyries include those of (quartz) syenite, biotite-K-feldspar and quartz-albite [26,28,43–45], yet they are rarely exposed in the Beiya mining district. Major exposed rocks in the Beiya deposit include the Lower Triassic Qingtianbao Formation (175–350 m thick), the Middle Triassic Beiya Formation and Quaternary sedimentary rocks (Figure 2). The Lower Triassic Qingtianbao Formation comprises arkose, hornfelsed greywacke, sandstone and basaltic volcanoclastic rocks, whereas the main ore-bearing Middle Triassic Beiya Formation comprises dolomitic, ferruginous, bioclastic and argillaceous limestone (ca. 138–531 m thick). The Beiya Formation is deposited in a NS-trending basin upon which a broad NS-trending syncline is developed [28].

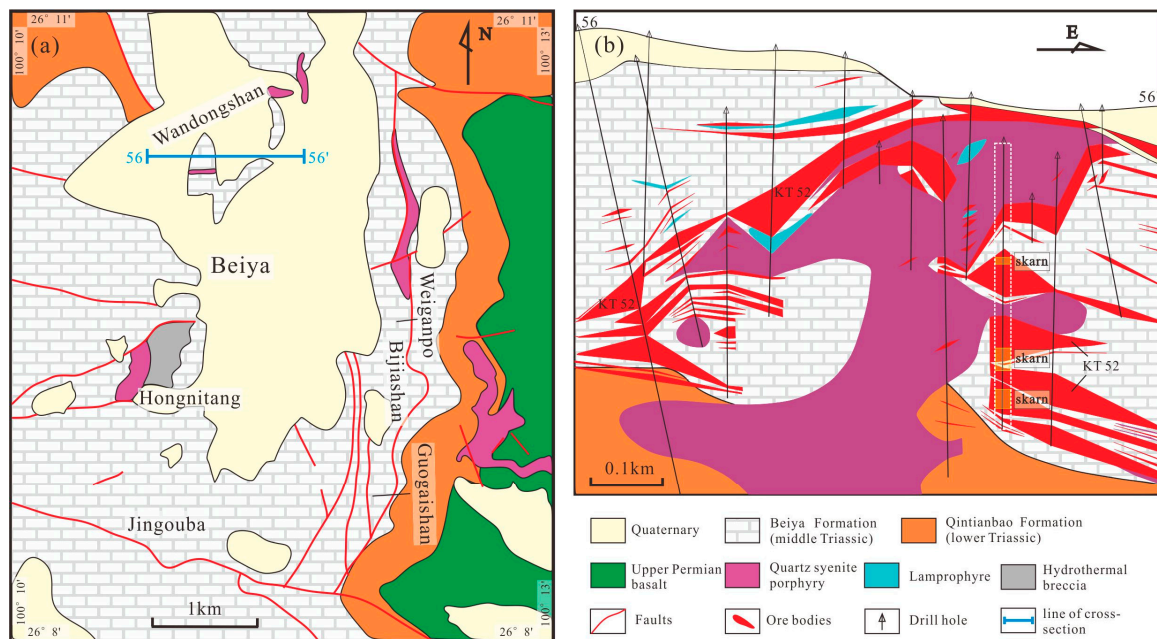


Figure 2. Geological map (a) and cross-section (b) of the Beiya deposit. Modified after [30,46].

Outcropping rocks in the Machangqing deposit include the Lower Ordovician Xiangyang Formation (O_1x), dolomitic limestone of the Lower Devonian Kanglang Formation (D_1k) and limestone of the Lower Devonian Qingshan Formation (D_1q) (Figure 3). The Xiangyang Formation comprises littoral-facies clastic rocks and contains four members, among which the third (O_1x^3) and fourth (O_1x^4) member are exposed in the ore field. O_1x^3 comprises grayish-green fine-grained sandstone with dark-gray shale in the upper part, and white fine-grained quartz sandstone with minor shale in the lower part. Unit O_1x^4 comprises quartz siltstone with limestone bands/lenses (main ore host) in the upper part, and coarse-grained feldspar-quartz sandstone with conglomerate, gravel-bearing gritstone and argillaceous siltstone lenses in the lower part. Permian basalts are also exposed in the northern part of the Machangqing deposit (Figure 3). During the Cenozoic Himalayan orogeny, multiple intrusions were emplaced in the area from 55.5 to 23.2 Ma [32]. These intrusive rocks are mainly composed of alkaline intrusions including syenite porphyry, quartz syenite porphyry, monzonite porphyry, granite porphyry, porphyritic granite and lamprophyre [30,35,36]. Among these porphyries, the alkaline granite porphyry (37.9–35.0 Ma) is considered to be ore-related [34,35,47,48]. The Machangqing intrusive complex was emplaced in the Xiangyang Formation at the onset of the mineralization.

Cenozoic tectonic evolution of the Jinshajiang–Ailaoshan suture is generally interpreted to comprise three stages: (1) India–Asia continent–continent collision started at ca. 55–50 Ma [49,50]; (2) northward indentation of the Indian plate caused the transition from “soft” to “hard” collision at 45 Ma, as evidenced by a reduction in the convergence rate (e.g., [51]); and (3) the collisional strain was accommodated by the lateral extrusion (i.e., escape tectonics) of the Indochina–Simao Block from ca. 32 Ma onward, and the Jinshajiang–Ailaoshan suture was reactivated as a regional strike-slip fault [52]. The Beiya and the Machangqing deposits were products of this Himalayan collisional tectonic event.

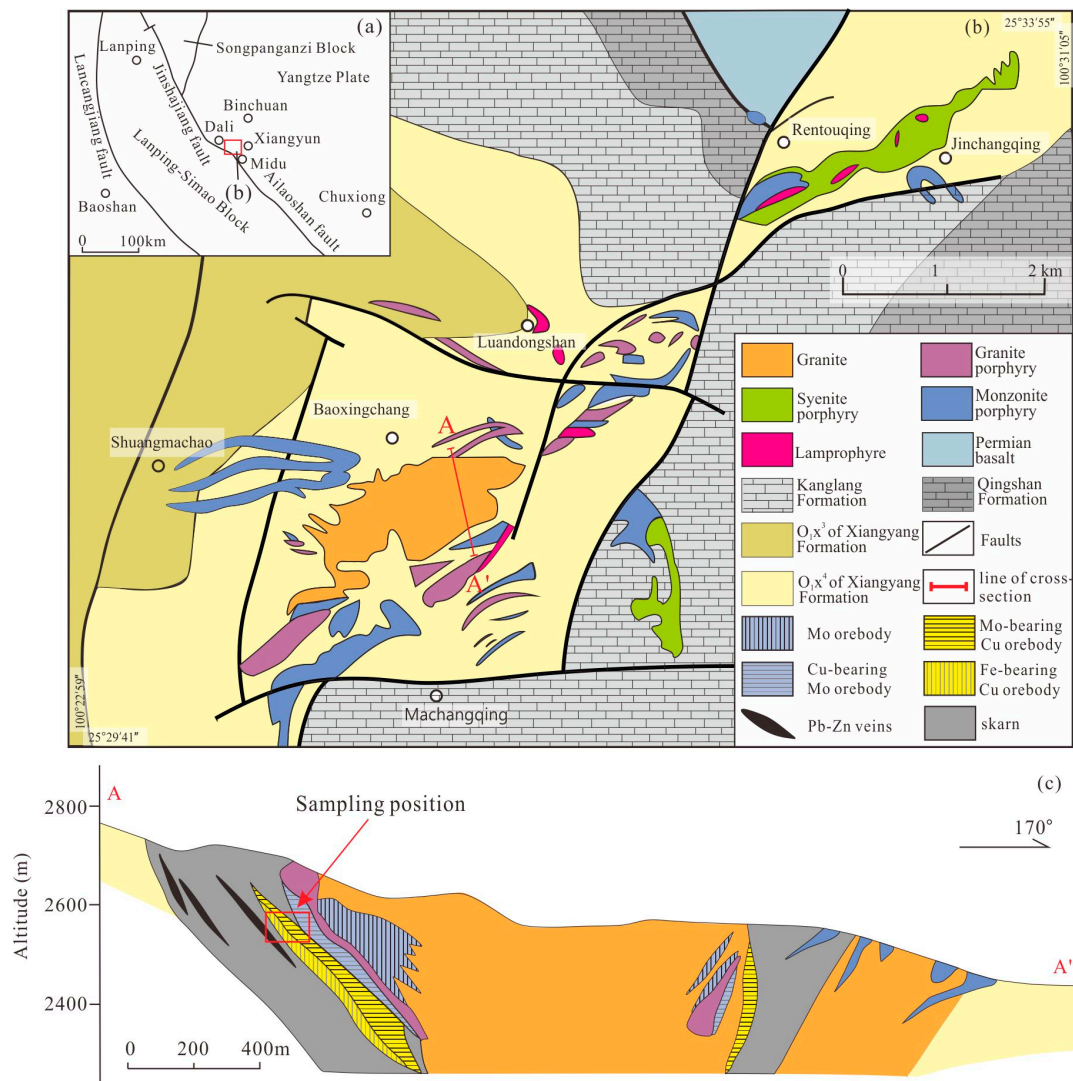


Figure 3. Geological map (a,b) and cross-section (c) of the Machangqing deposit. Modified after [30,45].

2.2. Ore Deposit Geology

2.2.1. Beiya

The Beiya Au-polymetallic deposit (~90 km north of Dali) is the largest gold skarn deposit in China. The deposit is located in the middle part of the Jinshajiang–Ailaoshan alkaline porphyry metallogenic belt [53] (Figure 1) and contains six ore segments, namely the Weiganpo, Bijiashan and Guogaishan segments in the east and the Wandongshan, Hongnitang and Jingouba segments in the west (Figure 2a). The Wandongshan (mainly the KT52 ore body) ranks the biggest, containing most of the Au resources (99 Mt @ 2.61 g/t Au [25]) and is currently being mined for gold and iron.

The orebodies in the Beiya deposit mostly occur in and/or along the contact zones between the intrusions and the carbonate host rocks of the Beiya Formation. Some stratiform orebodies are locally distributed along the flat interlayer fractures and breccia zones within the Beiya Formation carbonates, as well as at the contact of the carbonates and the underlying Qingtianbao Formation sandstone. Vein-like orebodies occur within the porphyritic intrusions, and laterite-hosted orebodies have also been documented [54]. Based on previous studies, the mineralization style in the Beiya deposit can be divided into porphyry, skarn and supergene styles [55]. Of these, skarn is the major mineralization type at Beiya deposit, with orebodies mostly found along the intrusive contact between

porphyries and the Beiya Formation carbonates. Orebody KT52 (around the Wandongshan porphyry) is the largest skarn orebody (Figure 2b), with proven reserves of 87.2 Mt Au @ 2.35 g/t, along with 90.27 Mt Fe @ 34 wt %, and 111.8 Mt Cu @ 0.34 wt % [54].

The dominant skarn mineralization comprises three stages: (1) prograde skarn; (2) retrograde alteration; and (3) quartz-sulfide stages. Minerals in the prograde skarn stage are mainly anhydrous, such as garnet and pyroxene (Figure 4a), whereas retrograde alteration minerals are predominantly hydrous (Figure 4b,c), including epidote, allanite, biotite and chlorite. Magnetite, titanite, scheelite, feldspar (including plagioclase and albite) and fluorite can also be found in the retrograde alteration stage. The quartz-sulfide stage (Figure 4d) is characterized by pyrite, chalcopyrite, pyrrhotite and molybdenite. Both the late retrograde alteration (quartz-magnetite) and quartz-sulfide stages are associated with the gold mineralization. The supergene orebodies with gold-bearing hematite and limonite are found along the unconformity between the Beiya Formation and the overlying Quaternary sediments. The porphyries emplaced in the Beiya deposit include those of quartz syenite, quartz monzonite, biotite orthoclase and quartz albite. Lamprophyre dikes are also documented in the area. Most of the porphyries were emplaced at around 36.9 to 33.3 Ma [24–26,28,56–60], except for the quartz albite porphyry (65 Ma) and the biotite orthoclase porphyry (3.8 Ma) [45]. The quartz syenite porphyry in the Beiya deposit has been LA-ICP-MS zircon U-Pb dated to be 36.07 ± 0.43 Ma [24], and the retrograde-stage hydrothermal titanite yielded a weighted average $^{206}\text{Pb}/^{238}\text{U}$ age of 33.1 ± 1.0 Ma [61]. Molybdenite from the Beiya Au skarn has yielded a Re-Os isochron age of 34.7 ± 1.6 Ma, which constrains the age of the quartz-sulfide stage mineralization [24].

In the Beiya deposit, gold mainly occurs as native gold and electrum in fractures and/or as vein-filling in pyrite, magnetite, limonite and quartz. In the retrograde alteration and quartz-sulfide stages, the gold is also hosted by magnetite and sulfides (pyrite, chalcopyrite and bismuthinite), respectively. Compositions of the Beiya skarn minerals suggest a typical oxidized skarn system [28]. Fluid inclusion studies indicate medium to high temperatures (186–372 °C) and high salinities (7.5–19.8 wt % NaCl equiv.) for the ore-forming fluids, which were likely originated from the magma with late-stage meteoric water involvement [62]. The $\delta^{34}\text{S}$ values of the quartz-sulfide stage range from -2.4‰ to 4.5‰ , suggesting that the ore-forming fluids were derived from and/or modified by the magma [54,62,63]. The $\delta^{18}\text{O}$ and δD compositions of the ore-forming fluids in the quartz-sulfide stage are -0.85‰ to 3.52‰ and -78.6‰ to -88.6‰ , respectively [62]. The isotope evidence suggests that the Beiya ore-forming materials were derived from deep-sourced magmas [54,62].

2.2.2. Machangqing

The Machangqing deposit is a porphyry Cu-Mo deposit with skarn and epithermal Cu, Mo, Fe, Au and Pb-Zn mineralization. The ore reserve is estimated to contain 39 Mt Cu at 0.64% and 56 Mt Mo at 0.08% [23]. The mineralized zone comprises five NE-trending ore segments, namely Shuangmacao, Baoxingchang, Luandongshan, Rentouqing and Jinchangqing.

The mineralization of the Machangqing deposit includes porphyry Cu-Mo mineralization (the Baoxingchang and Luandongshan ore segments), skarn Cu-Mo-Fe mineralization along the intrusive contacts (the Baoxingchang and Luandongshan ore segments) and epithermal Au-Pb-Zn mineralization in the Xiangyang and Kanglang formations (the Shuangmacao, Rentouqing and Jinchangqing ore segments [30,32]). These three mineralization styles form a complete alkalic porphyry-related mineral system, and show a systematic alteration and mineralization style transition from the intrusion to the wall rocks [30,32]. In the Machangqing deposit, the porphyry ores usually occur as Cu-Mo veinlets within the intrusion associated with potassic, phyllic and argillic alterations [23]. The skarn mineralization mainly comprises three major stages: (1) prograde skarn; (2) retrograde alteration; and (3) a quartz-sulfide mineralization. Prograde skarn minerals are mainly anhydrous (e.g., garnet and pyroxene) (Figure 4e), whereas the retrograde alteration minerals are mainly hydrous (e.g., epidote-group minerals, biotite and chlorite) (Figure 4f). Magnetite mineralization mainly occurred during the late retrograde alteration (quartz-magnetite)

stage, whilst the quartz-sulfide stage contains mainly pyrite, chalcopyrite and molybdenite (Figure 4g,h), and constitutes the main Cu-Mo mineralization stage. Previous studies have shown that the ore-forming temperature, pressure and salinities of the ore-forming fluids decreased from the porphyry, through skarn and to the epithermal mineralization [32,64]. The metal and fluid sources also changed from dominantly magmatic to hydrothermal [32]. The molybdenite Re-Os ages of the porphyry mineralization range from 33.9 ± 1.1 Ma to 35.8 ± 1.6 Ma [23,33–35,65].

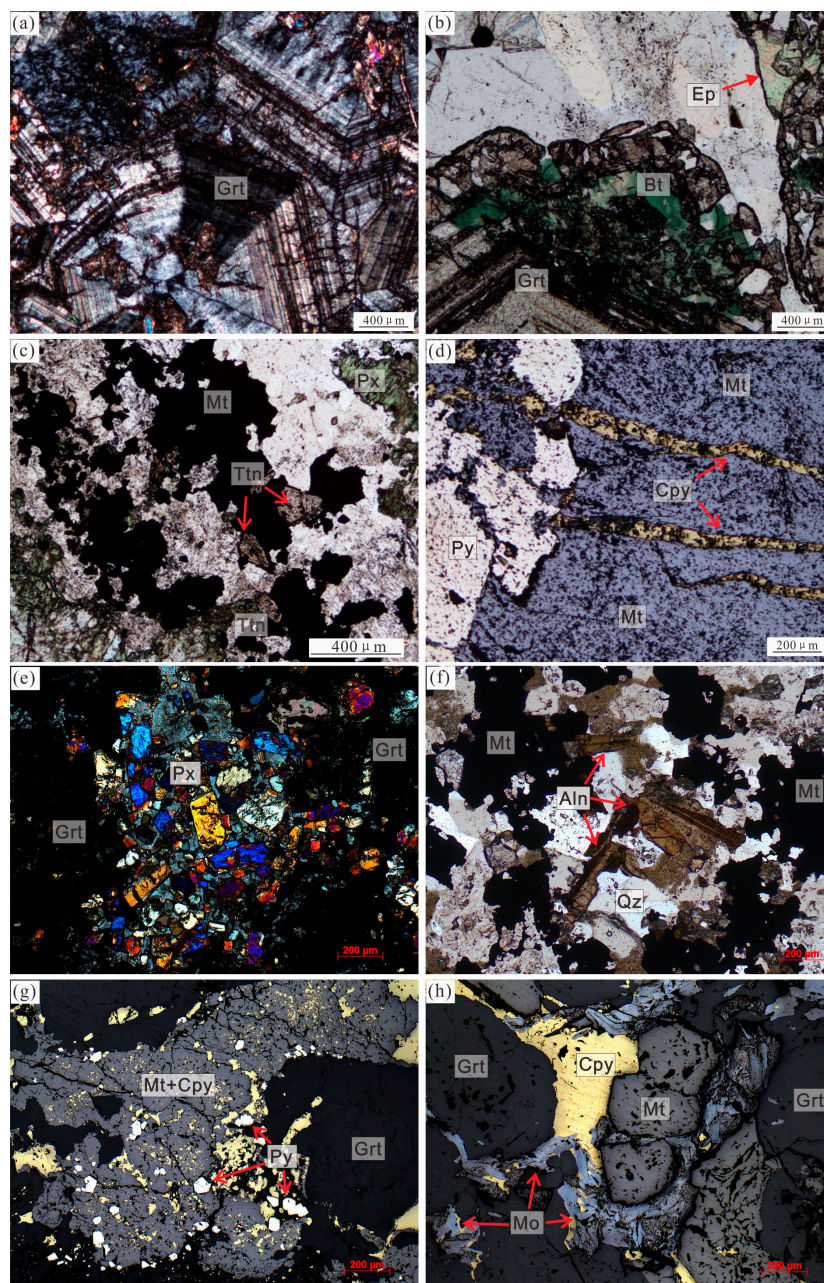


Figure 4. Photomicrographs of samples from different ore forming stages in: the Beiya deposit (a–d); and the Machangqing deposit (e–h) ((a,e) prograde skarn (garnet + pyroxene) mineral assemblage (cross-polarized light); (b,c,f) retrograde alteration (allanite + titanite + magnetite + biotite + quartz) mineral assemblage (plane-polarized light); and (d,g–h) quartz-sulfide mineralization (pyrite + chalcopyrite + magnetite + molybdenite) mineral assemblage (reflected light)). Abbreviations: Aln, allanite; Bt, biotite; Cpy, chalcopyrite; Ep, epidote; Grt, garnet; Mo, molybdenite; Mt, magnetite; Px, pyroxene; Py, pyrite; Qz, quartz; Ttn, titanite.

3. Samples and Analytical Methods

Allanite samples for the in-situ LA-ICP-MS U-Pb dating and trace element analysis were collected from the mineralized skarn (exoskarn) in the Beiya deposit (Wandongshan ore segment) and Machangqing deposit (Baopingchang ore segment). The allanite samples from the Beiya deposit occur in a mineral assemblage of garnet, pyroxene, magnetite, epidote, feldspar and quartz, with minor titanite and scheelite, whereas those from the Machangqing deposit occur in a mineral assemblage of pyroxene, magnetite, feldspar, quartz, chalcopyrite and calcite, with minor titanite and scheelite. Petrographic thin sections were prepared for all the samples, and were studied with optical microscopy and Back-Scattered Electron (BSE) imaging, using a Zeiss SIGMA field-emission Scanning Electron Microprobe (SEM) (Oberkochen, Germany) at the School of Earth Science and Geological Engineering of Sun Yat-sen University (Guangzhou, China). Prior to the LA-ICP-MS analysis, major element abundance of the allanite samples was determined on thin sections using a JEOL JXA-8230 electron probe micro-analyzer (EPMA) (Tokyo, Japan) at the Key Laboratory of Mineralogy and Metallogeny in the Guangzhou Institute of Geochemistry, Chinese Academy of Sciences (GIGCAS). Operating conditions include 15 kV accelerating voltage, 20 nA beam current and a beam diameter of 2 μm .

In-situ U-Pb dating and trace element analyses of allanite were performed by LA-ICP-MS at the Key Laboratory of Marine Resources and Coastal Engineering, Sun Yat-sen University. The analyses were performed using a 193 nm ArF excimer laser ablation system (*GeoLasPro*) coupled with an Agilent 7700x ICP-MS (Santa Clara, CA, USA). A 32 μm spot size was used with an energy density of 5 J/cm² and a repetition rate of 5 Hz. The trace element compositions of allanite were calibrated against the Standard NIST610 [66], using Si determined by EPMA as the internal standard. Zircon 91500 [67] was used as the external standard for the U-Pb dating. A sample-standard bracketing method was used for instrumental drift correction. Each analysis consists of a 20 s background measurement (laser-off) followed by 45 s of data acquisition. Data reduction was performed using ICPMSDataCal software [68]. Time-dependent drifts of U-Th-Pb isotopic ratios were corrected using a linear interpolation (with time) for every five analyses based on the variations of 91500 zircon standard, and the detailed procedure can be found in literature [68]. ISOPLLOT 3.0 software [69] was used to construct the Tera-Wasserburg diagram and isochrons.

Allanite commonly have large initial common Pb contents. Therefore, attention should be paid in correcting Pb isotopic data, and the choice of initial Pb isotopic composition would significantly influence the calculated ages [4]. We adopted the ²⁰⁷Pb correction method, which has been widely used to determine the age of relatively young allanite [4,70]. The ²⁰⁴Pb correction is less precise, because the counting error on ²⁰⁴Pb is larger than on the more abundant ²⁰⁷Pb. ²⁰⁴Pb is also more susceptible to measurement error due to isobaric interference. The uncorrected data are plotted on the Tera-Wasserburg diagram, and a regression through these analyses yields a lower intercept that represents the apparent allanite age. The y-intercept represents the initial ²⁰⁷Pb/²⁰⁶Pb, which can be used for the ²⁰⁷Pb-correction. The amount of common ²⁰⁶Pb is expressed as a fraction of the total ²⁰⁶Pb (*f*₂₀₆), which can be calculated from:

$$f_{206} = \frac{{}^{206}\text{Pb}_c}{{}^{206}\text{Pb}_m} = \frac{{}^{207}\text{Pb}/{}^{206}\text{Pb}_m - {}^{207}\text{Pb}/{}^{206}\text{Pb}^*}{{}^{207}\text{Pb}/{}^{206}\text{Pb}_c - {}^{207}\text{Pb}/{}^{206}\text{Pb}^*} \quad (1)$$

where ²⁰⁷Pb/²⁰⁶Pb_m is the measured ratio, ²⁰⁷Pb/²⁰⁶Pb* is the expected radiogenic ratio for the inferred age and ²⁰⁷Pb/²⁰⁶Pb_c is the common Pb composition (the initial ²⁰⁷Pb/²⁰⁶Pb).

For the Th-Pb system, isochrons can be constructed from multiple analyses of allanite samples which could be constructed with common ²⁰⁶Pb (²⁰⁶Pb_c) as the reference stable isotope:

$${}^{232}\text{Th}_m/{}^{206}\text{Pb}_c = \frac{{}^{232}\text{Th}/{}^{206}\text{Pb}_m}{f_{206}} \quad (2)$$

$${}^{208}\text{Pb}_m/{}^{206}\text{Pb}_c = \frac{{}^{208}\text{Pb}/{}^{206}\text{Pb}_m}{f_{206}} \quad (3)$$

where $^{232}\text{Th}/^{206}\text{Pb}_m$ and $^{208}\text{Pb}/^{206}\text{Pb}_m$ are the measured ratios. The isochrons can be constructed as below:

$$^{208}\text{Pb}_m/^{206}\text{Pb}_c = ^{208}\text{Pb}/^{206}\text{Pb}_c + ^{232}\text{Th}_m/^{206}\text{Pb}_c \times (e^{\lambda^{232}\text{t}} - 1) \quad (4)$$

where $^{208}\text{Pb}/^{206}\text{Pb}_c$ is the initial common Pb composition, which can be determined from the intercept of the isochron. The age of allanite can be calculated from the slope of the isochron. This approach has been shown to be effective for correcting common-Pb in allanite.

The allanite in the Beiya and Machangqing mineralized skarn comprise euhedral to subhedral crystals (Figure 5a–f). Allanite grains in the Beiya deposit are typically 50–300 μm in length (Figure 5a,c,d) and exhibit obvious pleochroism under the microscope. They associate with skarn minerals such as garnet, pyroxene, magnetite, titanite, fluorite, feldspar and quartz, and mostly occur in the core of altered garnet (Figure 5c). Allanite from the Machangqing mineralized skarn is similar with the Beiya deposit, most of which is 50–400 μm in length and occurs with magnetite, chlorite, chalcopyrite, calcite and quartz (Figure 5b,e,f). All the allanite grains from both the Beiya and Machangqing deposits are often closely intergrown with magnetite (Figure 5a,b), and some fractures in the magnetite are filled with sulfides (Figure 4d). This indicates that the allanite was syn-magnetite mineralized, followed by sulfide mineralization. No obvious patchy zoning or overgrowth texture was observed in the allanite from the Beiya and Machangqing deposits under BSE imaging, suggesting a single growth phase (Figure 5c–f).

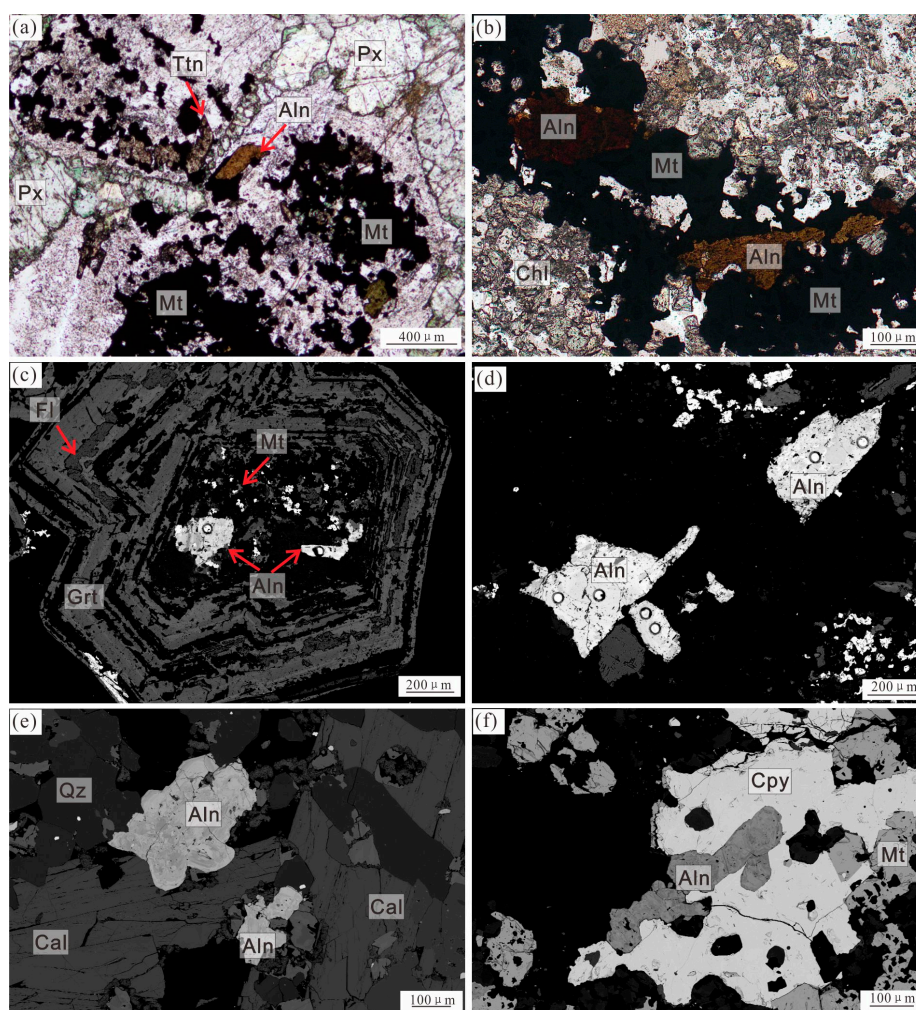


Figure 5. Photomicrographs and BSE images of the allanite from: the Beiya deposit (a,c,d); and the Machangqing deposit (b,e,f). Abbreviations: Aln, allanite; Cal, calcite; Chl-, chlorite; Cpy, chalcopyrite; Fl, fluorite; Grt, garnet; Mt, magnetite; Px, pyroxene; Py, pyrite; Qz, quartz; Ttn, titanite.

4. Results

4.1. Major and Trace Elements of Allanite

The major element compositions of the Beiya and Machangqing allanite are summarized in Table A1, and the chemical formula of allanite was calculated based on the total cation number as 8 (12.5 O basis). Fe^{3+} is calculated using the equation $(\text{Fe}^{3+}/(\text{Fe}^{2+} + \text{Fe}^{3+})) = ((\text{REE}^{3+} + \text{Th}^{4+})/(\text{Al}^{3+} - 3)) + 1$ [71]. Allanite in the Beiya and Machangqing skarn have uniform SiO_2 (30.6–32.9 wt % and 30.2–32.8 wt %, respectively) and high FeO contents (average 21.5 wt % and 21.0 wt %, respectively). All the Beiya and Machangqing allanite samples contain very high concentrations of light rare earth element (LREE), with the average La_2O_3 content of 8.35 and 7.25 wt %, and the average Ce_2O_3 content of 8.16 and 9.61 wt %, respectively. The Beiya allanite contains higher ThO (average: 0.41 wt %) and $\text{Fe}^{3+}/(\text{Fe}^{2+} + \text{Fe}^{3+})$ (average: 0.66 wt %) than the Machangqing allanite (average: 0.09 wt % and 0.63 wt %, respectively). The strongly positive $(\text{REE} + \text{Fe}^{2+} + \text{Mg})$ vs. $(\text{Ca} + \text{Al} + \text{Fe}^{3+})$ correlation (Figure 6) indicates that a substitution mechanism of $\text{REE}^{3+} + (\text{Fe}^{2+}, \text{Mg}^{2+}) - \text{Ca}^{2+} + (\text{Al}^{3+}, \text{Fe}^{3+})$ operated in allanite [13].

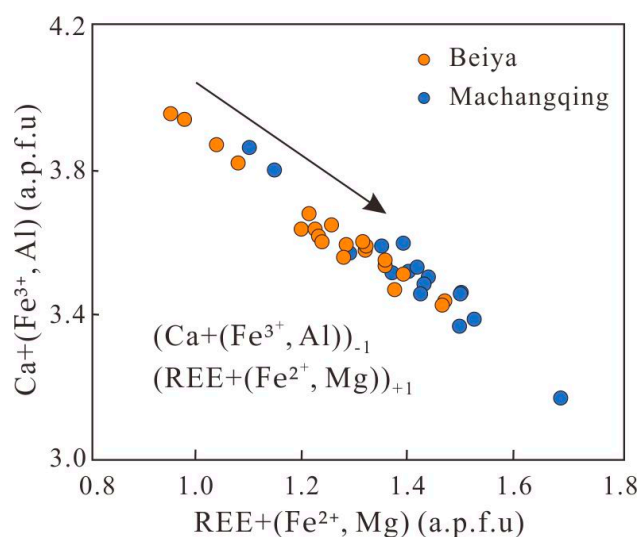


Figure 6. Major element plots of the Beiya and Machangqing allanite, showing negative $(\text{REE} + \text{Fe}^{2+} + \text{Mg})$ vs. $(\text{Ca} + \text{Al} + \text{Fe}^{3+})$ correlation. The line defines the 1:1 substitution of $\text{REE}^{3+} + (\text{Fe}^{2+}, \text{Mg}^{2+})$ for $\text{Ca}^{2+} + (\text{Al}^{3+}, \text{Fe}^{3+})$ in allanite.

Trace element geochemical analysis (Table A2) show that the Beiya allanite is significantly more U-rich (78–591 ppm, average: 172 ppm) than the Machangqing allanite (23–145 ppm, average: 78 ppm) (Figure 7a), and that the Th/U ratios of the Beiya allanite (average: 26.1) are also higher than its Machangqing counterpart (average: 12.9) (Figure 7b). Chondrite-normalized REE patterns of the Beiya and Machangqing allanite are shown in Figure 8. The Beiya and Machangqing allanite displays similar REE patterns with elevated total REE (ΣREE) contents (average ΣREE : 170,963 ppm and 149,772 ppm, respectively). They are characterized by significant LREE enrichment (LREE/HREE: 170–437 (Beiya) and 236–1439 (Machangqing)) and negative Eu anomalies (δEu : 0.24–0.40 (Beiya) and 0.30–0.57 (Machangqing)). Comparatively, the Beiya allanite has higher ΣREE content, but lower δEu and LREE/HREE ratio than the Machangqing allanite (Figure 7b,c).

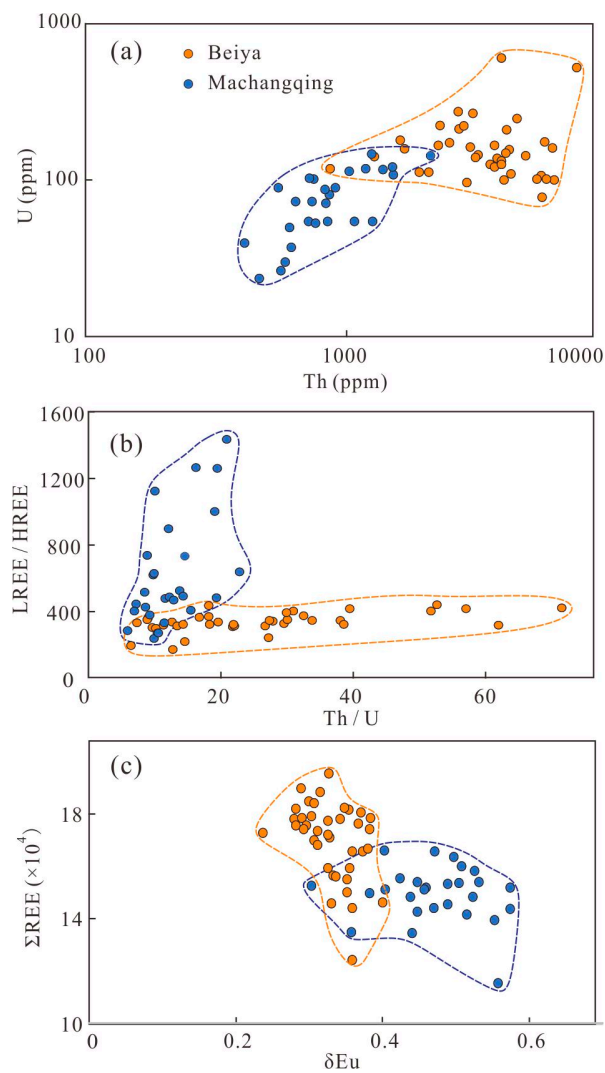


Figure 7. Plots of: (a) Th vs. U; (b) Th/U vs. LREE/HREE (light rare earth element divide heavy rare earth element); and (c) total REE (ΣREE) vs. δEu in the allanite from the Beiya and Machangqing deposits.

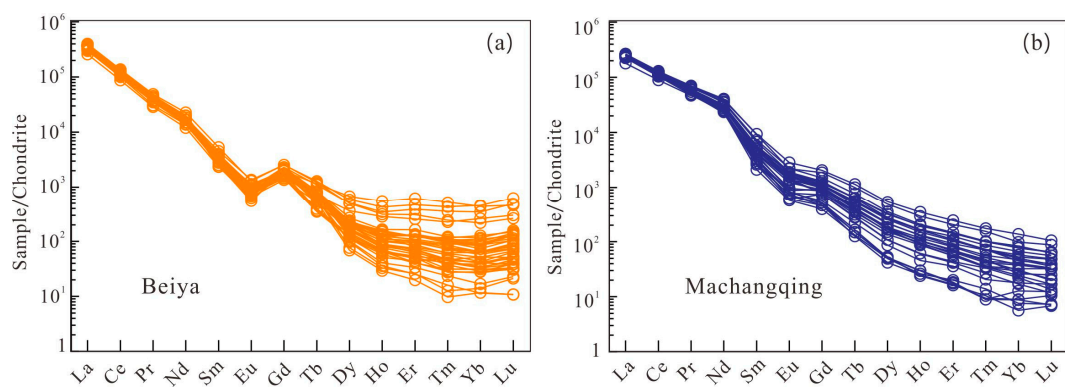


Figure 8. Chondrite-normalized REE patterns of allanite from the (a) Beiya and (b) Machangqing deposits. Normalizing values are from [72].

4.2. Allanite U-Th-Pb Ages

The corrected U-Pb isotope results of allanite from the Beiya and Machangqing deposits are presented in Table A3. In the Tera-Wasserburg diagram, the common Pb-uncorrected data of the Beiya and Machangqing allanite define a linear array, giving a lower-intercept age of 42.1 ± 4.7 Ma (MSWD = 4.2) and 35.4 ± 5.5 Ma (MSWD = 2.3), respectively. The Y-intercept of initial $^{207}\text{Pb}/^{206}\text{Pb}$ is 0.864 and 0.826, respectively (Figure 9). The Th-Pb isochrons of the Beiya and Machangqing allanite samples are shown in Figure 10, giving the $^{208}\text{Pb}/^{206}\text{Pb}_{\text{c}}$ results of 2.760 and 1.946, with the Th-Pb isochron ages of 33.4 ± 4.6 Ma (MSWD = 0.22) and 35.4 ± 9.8 Ma (MSWD = 0.26), respectively.

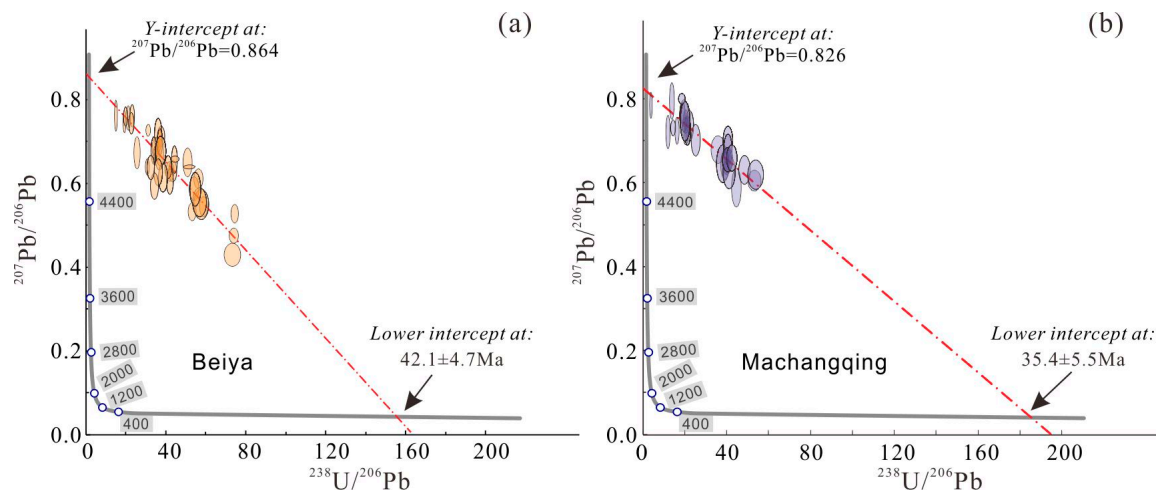


Figure 9. Laser ablation-inductively coupled plasma-mass spectrometry (LA-ICP-MS) Tera-Wasserburg diagram: (a) the Beiya deposit; and (b) the Machangqing deposit.

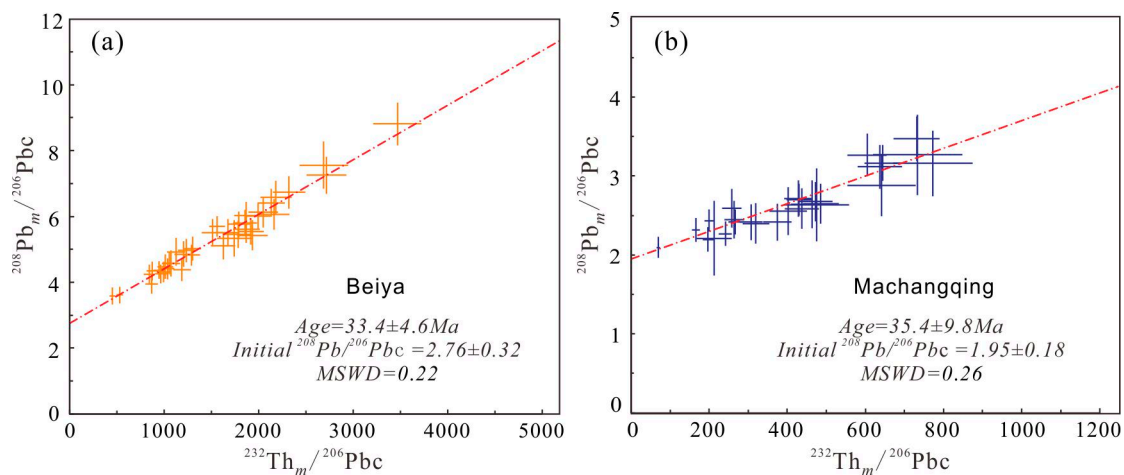


Figure 10. LA-ICP-MS Th-Pb isochrons of the allanite samples from: (a) the Beiya deposit; and (b) the Machangqing deposit.

5. Discussion

5.1. Reliability of Allanite U-Th-Pb Dating

Previous studies [4,14,16,73] show that precise allanite U-Th-Pb dating is influenced by several factors: (1) high and variable common Pb content; (2) excess ^{206}Pb from ^{230}Th decay in high-Th samples; and (3) lack of suitable matrix-matched allanite standards due to the large compositional variations caused by the solid solution with epidote.

Both the U-Pb and Th-Pb systems can be used to date allanite, although, in many cases, the latter is preferable due to its high Th content [14]. The correction for incorporation of ^{230}Th during the mineral's growth is often necessary for young allanite, because the excess ^{206}Pb from the ^{230}Th decay in Th-rich minerals can affect the $^{206}\text{Pb}/^{238}\text{U}$ and $^{207}\text{Pb}/^{235}\text{U}$ ages of the young samples [4,14,18]. Excess ^{206}Pb results in older apparent concordia intercept ages and lower $^{207}\text{Pb}/^{206}\text{Pb}$ values for the common Pb component in the y-intercept. The elevated intercept age reflects the variable ^{206}Pb excess (Figure 9). Therefore, we use the Th-Pb system and choose the Th-Pb isochron ages as the real age of the allanite samples. Compared to the Beiya allanite, the Machangqing allanite yielded an intercept age closer to the Th-Pb isochron age because of its lower Th content (Figures 9 and 10). In addition, the larger analytical uncertainty of Th-Pb isochron ages for the Machangqing allanite may have resulted from the lower Th and ^{208}Pb contents than the Beiya allanite (Table A2).

Some studies suggest that LA-ICP-MS analysis is less sensitive to matrix effect than ion-microprobe analysis [4]. In many cases, using an allanite standard for the external calibration of U-Th-Pb ages may not be imperative due to the compositional difference between the samples and the reference materials. Completely matrix matched materials are rare because allanite has a much greater range of elemental substitution than many other minerals used for U-Th-Pb dating (e.g., monazite), and even the most widely-used allanite reference materials (e.g., AVC and Tara) have large variations in common-Pb content [4]. Many previous studies have shown that accurate and precise allanite U-Th-Pb ages can be obtained by using non-matrix matched external standards, such as zircons (91500 and GJ-1) [11,12,14,17] and synthetic glass (NIST610) [18]. Therefore, the non-matrix matched external standardization approach with the use of zircon standard 91500 in this study is likely to be reliable.

5.2. Age of Skarn Mineralization in the Beiya and Machangqing Deposits

Different origins of allanite can be discriminated by their paragenetic mineral assemblages and geochemistry [9]. In general, hydrothermal allanite contains lower Th/U (mostly < 50) than magmatic allanite (mostly > 50) due to the higher mobility of U in hydrothermal fluids than Th [74]. Both the Beiya and Machangqing allanite yielded relatively low Th/U ratios (average: 25.5 and 12.9, respectively), which rules out a magmatic origin. Besides, the allanite from the Beiya and Machangqing deposits commonly coexists with skarn minerals (e.g., magnetite, garnet, feldspar and pyroxene), suggesting a hydrothermal origin.

Paragenetic evidence indicates that the Beiya and Machangqing allanite were formed during the retrograde alteration stage before the quartz-sulfide stage, which implies that the hydrothermal allanite ages at Beiya and Machangqing were broadly coeval with the magnetite mineralization but slightly older than the sulfide mineralization. Thus, the U-Th-Pb ages of the hydrothermal allanite from the Beiya and Machangqing deposits provide an upper age limit of mineralization at 33.4 ± 4.6 Ma and 35.4 ± 9.8 Ma, respectively.

Previous studies suggested that the Beiya ore-related porphyry were formed at 36.1 ± 0.4 Ma [24], and that the titanite U-Pb age and the molybdenite Re-Os age have altogether constrained the Beiya Au skarn mineralization to ca. 33.1–34.1 Ma [61]. In this study, the skarn mineralization is determined to be largely coeval with the Au mineralization, and slightly younger than the porphyry emplacement. Meanwhile, the ore-related granite porphyries in the Machangqing deposit were zircon U-Pb dated to be ca. 35.0–37.9 Ma [34,35,47,48], and the porphyry mineralization was molybdenite Re-Os dated to be ca. 33.9–35.8 Ma [23,33–35,65], which are broadly coeval with the skarn mineralization (determined by allanite U-Th-Pb dating in this study). The similar ages between the porphyry and skarn mineralization in the Machangqing deposit suggest that they were likely formed in the same metallogenic system, and that the alkaline granite porphyry had likely supplied the ore-forming materials, fluids and heat that drove the mineralization. As a whole, the skarn mineralization in the Beiya and Machangqing deposits are synchronous and temporally related to the magmatic hydrothermal activity in the Himalayan orogenic event. Besides, the marked similarity between our new Beiya allanite U-Th-Pb

age (33.4 ± 4.6 Ma) and the published Beiya titanite U-Pb age (33.1 ± 1.0 Ma) [61] suggests that our U-Th-Pb dating and data reduction approach are reliable.

5.3. Metallogenic Implications

The U contents of allanite can be used to evaluate the oxygen fugacity (fO_2) of the ore-forming fluids [12,13]. Uranyl (U^{6+}) complexes are strongly soluble in hydrothermal fluids [13], and therefore highly U contents may indicate more oxidized fluids [12]. The Beiya allanite has higher U contents (average: 171 ppm) than the Machangqing allanite (average: 78 ppm) (Figure 7a), suggesting that the ore-forming fluids in the Beiya deposit may have been more oxidized. This conclusion is also supported by the higher $Fe^{3+}/(Fe^{3+} + Fe^{2+})$ ratios of the Beiya allanite (Figure 11). The allanite in the Beiya deposit is co-precipitated with magnetite during the retrograde stage, which predate the gold discharge at quartz sulfide stage [75], and the oxygen fugacity revealed by allanite should represent for the quartz-magnetite stage that recharging and/or migration the gold-bearing fluid. Similarly, the mineral assemblage of allanite and magnetite in the Machangqing deposit predated the precipitation of copper during the sulfide stage. The oxygen fugacity of allanite from the Machangqing deposit could provide constrain for the oxidation state of Cu-bearing fluid in the quartz-magnetite (retrograde) stage.

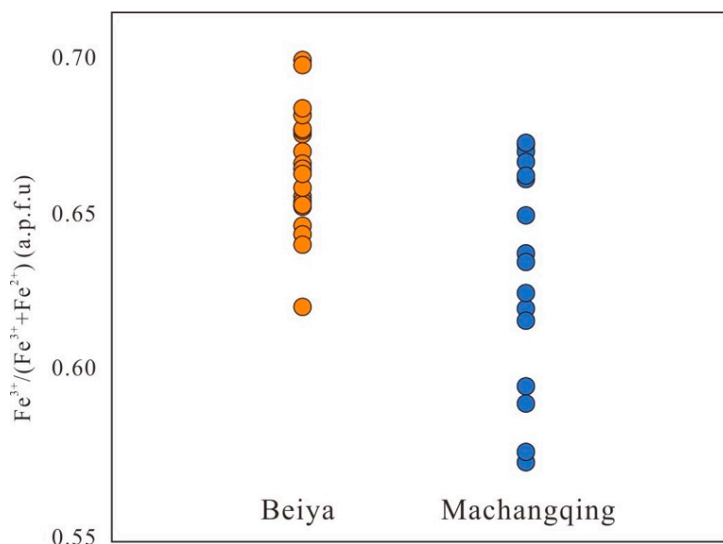


Figure 11. $Fe^{3+}/(Fe^{3+} + Fe^{2+})$ ratios of allanite from the Beiya and Machangqing deposits.

Previous studies show that in chloride-rich hydrothermal fluids, Th is much less soluble than U, yet both U and Th are highly soluble in F-rich fluids [11,76]. Thus, enrichments of F^- ligands in the hydrothermal fluids would cause high-Th allanite precipitation [11,13,77]. The hydrothermal allanite from the Machangqing deposit contains much lower Th content (average: 914 ppm) than that from the Beiya deposit (average: 3630 ppm), suggesting higher F activities in the Beiya ore-forming fluids. This conclusion is consistent with the presence of fluorite in the Beiya Au skarn ores (Figure 5c). In summary, our new allanite geochemical data indicate a higher F content and oxygen fugacity for the ore-forming fluids in the Beiya deposit than those in the Machangqing deposit.

Although the giant Beiya Au deposit and Machangqing Cu-Mo deposit are both located in the middle part of the Jinshajiang–Ailaoshan metallogenic belt (about 100 km apart), they differ greatly in terms of the ore deposit size and types of metals. The higher oxygen fugacity in the Beiya magmatic fluids had likely prevented early sulfide precipitation and the consequent metal removal, as well as increased the metal solubility in the hydrothermal fluids [78]. As a result, the Beiya ore-forming fluids could carry more metals than its Machangqing counterparts, leading to a larger deposit size of the former. Besides, gold can be effectively transported as gold (III) fluoride in

high-temperature hydrothermal fluids [79], and the higher F^- content in the Beiya hydrothermal fluids (cf. the Machangqing ones) may lead to the Au-dominated mineralization in the Beiya deposit (and the sub-economic gold mineralization in the Machangqing deposit).

6. Conclusions

- (1) Allantite U-Th-Pb geochronology can be obtained by using Th-Pb isochron age and the non-matrix matched external standardization approach.
- (2) Allantite from the Beiya and Machangqing Au skarn yielded a Th-Pb isochron ages of 33.4 ± 4.6 Ma (MSWD = 0.22) and 35.4 ± 9.8 Ma (MSWD = 0.26), respectively, representing the ages of the retrograde alteration.
- (3) Major and trace element characteristics of the allantite from the two deposits suggest that the ore-forming fluids in the Beiya deposit may have had higher F content and oxygen fugacity than those in the Machangqing deposit.

Acknowledgments: This work was jointly funded by the National Natural Science Foundation of China (41602067, U1302233, and 41702067), Chinese Postdoctoral Science Foundation (2015M582457), National Key Basic Research Program (2015CB452604), Natural Science Foundation of Guangdong Province (2017A030313246), Pearl River Scholar Funded Scheme (2011), and the Fundamental Research Funds for the Central Universities (17lgpy63). We thank Changming Xing for helping with the EPMA analysis, and Wenchang Li for the fieldwork and sampling support. The academic editor David Chew and two anonymous reviewers are thanked for their constructive comments.

Author Contributions: Yu Fu and Xiaoming Sun conceived and designed the experiments; Yu Fu performed the experiments; Dengfeng Li and Hai Lin analyzed the data; Yu Fu wrote the paper, assisted by all other authors; and Lai Chunkit and Dengfeng Li contributed to the revising of the paper.

Conflicts of Interest: The authors declare no conflict of interest.

Appendix A

Table A1. Electron microprobe analysis results (wt %) of the Beiya and Machangqing allanite.

Beiya																					
Point	W364-1-01	W364-1-02	W364-1-03	W364-1-04	W364-1-05	W364-1-06	W364-1-07	W364-1-08	W364-1-09	W364-1-10	W364-1-11	W364-2-01	W364-2-02	W364-2-03	W364-2-04	W364-2-05	W364-2-06	W364-2-07	W364-2-08	W364-2-09	W364-2-10
MgO	0.30	0.32	0.33	0.41	0.33	0.31	0.34	0.33	0.33	0.30	0.35	0.31	0.30	0.33	0.33	0.34	0.30	0.33	0.37	0.37	0.34
Al ₂ O ₃	8.10	9.72	11.14	10.32	9.55	12.59	9.09	10.08	9.11	9.15	9.85	10.31	9.11	12.95	13.33	9.23	9.83	10.35	7.31	9.68	13.33
SiO ₂	30.59	31.32	31.82	31.19	31.51	32.73	30.97	31.84	31.02	30.74	31.35	31.96	31.64	32.89	32.79	31.89	31.42	31.49	30.94	31.23	32.58
CaO	12.06	12.82	13.69	12.77	13.40	15.05	12.73	13.83	12.59	12.16	13.11	13.81	13.28	15.78	15.61	13.32	13.38	13.48	12.44	13.16	15.92
TiO ₂	0.65	0.62	0.59	0.62	0.83	0.74	0.55	0.59	0.57	0.65	0.58	0.72	0.58	0.89	0.79	0.99	0.79	0.70	0.79	0.80	0.55
MnO	0.29	0.27	0.25	0.27	0.31	0.27	0.26	0.22	0.25	0.27	0.25	0.26	0.22	0.24	0.23	0.25	0.25	0.23	0.28	0.27	0.24
FeO _T	24.15	22.53	20.69	20.79	22.37	19.23	22.49	21.92	22.66	22.27	21.81	21.61	23.12	19.21	18.19	21.85	22.16	21.31	24.21	21.50	18.41
La ₂ O ₃	9.48	8.60	8.60	8.47	8.40	7.77	8.88	8.06	9.09	9.51	9.09	8.09	8.95	6.23	6.76	8.52	8.98	8.28	8.93	8.58	6.06
Ce ₂ O ₃	9.60	8.46	7.98	8.30	7.45	7.08	8.71	7.83	8.83	9.30	8.69	8.25	8.54	6.75	7.41	7.71	8.45	8.06	9.01	8.19	6.83
Pr ₂ O ₃	0.46	0.47	0.46	0.42	0.45	0.42	0.45	0.47	0.47	0.55	0.51	0.44	0.45	0.50	0.49	0.47	0.49	0.50	0.45	0.48	0.43
Nd ₂ O ₃	0.91	0.95	0.90	0.87	1.00	0.88	0.91	0.94	0.97	1.24	1.08	0.91	0.89	1.02	0.97	0.95	1.00	1.00	0.91	0.90	0.83
ThO ₂	0.37	0.54	0.27	0.28	1.43	0.10	0.53	0.68	0.72	0.42	0.26	0.28	0.42	0.32	0.38	0.30	0.24	0.37	0.08	0.25	0.37
F	0.18	0.12	0.38	0.35	0.18	0.11	0.16	0.11	0.10	0.19	0.14	0.41	0.08	0.01	0.10	0.01	0.11	0.09	0.22	0.14	0.21
Total	96.59	96.08	96.46	94.42	95.59	97.07	95.39	96.11	95.88	96.14	96.67	96.66	97.06	96.78	96.89	95.52	97.05	95.72	95.63	95.16	95.51
Formula Calculation Based on 8 Cations and 12.5 Oxygens																					
Mg	0.04	0.05	0.05	0.06	0.05	0.04	0.05	0.05	0.05	0.04	0.05	0.04	0.04	0.04	0.04	0.05	0.04	0.05	0.05	0.05	0.05
Al	0.93	1.09	1.22	1.16	1.07	1.36	1.03	1.12	1.04	1.04	1.11	1.13	1.02	1.39	1.43	1.04	1.10	1.16	0.84	1.10	1.43
Si	2.96	2.99	2.96	2.99	2.98	3.00	2.99	3.00	2.99	2.98	2.98	2.97	3.00	2.99	2.99	3.06	2.98	3.00	3.01	3.00	2.97
Ca	1.25	1.31	1.37	1.31	1.36	1.48	1.32	1.40	1.30	1.26	1.34	1.38	1.35	1.54	1.52	1.37	1.36	1.37	1.30	1.36	1.55
Ti	0.05	0.04	0.04	0.04	0.06	0.05	0.04	0.04	0.04	0.05	0.04	0.05	0.04	0.06	0.05	0.07	0.06	0.05	0.06	0.06	0.04
Mn	0.02	0.02	0.02	0.02	0.02	0.02	0.02	0.02	0.02	0.02	0.02	0.02	0.02	0.02	0.02	0.02	0.02	0.02	0.02	0.02	0.02
Fe ²⁺	0.69	0.62	0.56	0.58	0.58	0.49	0.63	0.56	0.65	0.68	0.63	0.55	0.62	0.45	0.47	0.56	0.61	0.58	0.63	0.59	0.43
Fe ³⁺	1.26	1.18	1.05	1.08	1.19	0.98	1.19	1.16	1.18	1.12	1.11	1.13	1.22	1.02	0.92	1.19	1.14	1.11	1.34	1.14	0.97
La	0.34	0.30	0.30	0.30	0.29	0.26	0.32	0.28	0.32	0.34	0.32	0.28	0.31	0.21	0.23	0.30	0.31	0.29	0.32	0.30	0.20
Ce	0.34	0.30	0.27	0.29	0.26	0.24	0.31	0.27	0.31	0.33	0.30	0.28	0.30	0.23	0.25	0.27	0.29	0.28	0.32	0.29	0.23
Pr	0.02	0.02	0.02	0.01	0.02	0.01	0.02	0.02	0.02	0.02	0.02	0.01	0.02	0.02	0.02	0.02	0.02	0.02	0.02	0.02	0.01
Nd	0.03	0.03	0.03	0.03	0.03	0.03	0.03	0.03	0.03	0.04	0.04	0.03	0.03	0.03	0.03	0.03	0.03	0.03	0.03	0.03	0.03
Th	0.01	0.01	0.01	0.01	0.03	0.00	0.01	0.01	0.02	0.01	0.01	0.01	0.01	0.01	0.01	0.01	0.01	0.01	0.00	0.01	0.01
F	0.05	0.04	0.11	0.11	0.05	0.03	0.05	0.03	0.03	0.06	0.04	0.12	0.02	0.00	0.03	0.00	0.03	0.03	0.07	0.04	0.06
Total	8.00	8.00	8.00	8.00	8.00	8.00	8.00	8.00	8.00	8.00	8.00	8.00	8.00	8.00	8.00	8.00	8.00	8.00	8.00	8.00	8.00
Fe ³⁺ / (Fe ²⁺ + Fe ³⁺)	0.65	0.65	0.65	0.65	0.67	0.67	0.65	0.67	0.64	0.62	0.64	0.67	0.66	0.70	0.66	0.68	0.65	0.66	0.68	0.66	0.69

Table A1. Cont.

Machangqing																
Points	JDS03-01A-01	JDS03-01A-02	JDS03-01A-03	JDS03-01A-04	JDS03-01A-05	JDS03-01A-06	JDS03-01A-07	JDS03-01A-08	JDS03-01B-01	JDS03-01B-02	JDS03-01B-03	JDS03-01B-04	JDS03-01B-05	JDS03-01B-06	JDS03-01B-07	JDS03-01B-08
MgO	0.65	0.64	0.69	0.44	0.65	0.60	0.45	0.89	0.81	0.90	0.81	0.89	0.82	0.80	0.81	0.84
Al ₂ O ₃	11.10	13.00	12.45	10.11	8.78	12.03	10.22	8.81	8.03	10.37	12.27	8.73	8.83	9.95	8.42	10.08
SiO ₂	31.60	32.81	31.55	31.13	30.15	31.34	31.22	30.32	30.48	31.52	32.48	30.60	30.99	31.20	30.54	31.16
CaO	13.16	15.28	13.14	12.91	12.03	13.35	12.93	11.71	11.76	13.28	15.24	11.97	12.40	13.13	11.31	12.67
TiO ₂	0.68	0.60	0.61	0.55	0.60	0.29	0.73	0.63	0.79	0.96	0.63	0.80	0.90	0.69	0.62	0.46
MnO	0.16	0.14	0.15	0.17	0.21	0.14	0.25	0.17	0.20	0.25	0.21	0.23	0.24	0.29	0.20	0.30
FeO _T	20.34	19.20	18.69	21.51	23.04	19.43	21.72	21.16	23.43	19.50	18.67	23.08	23.56	22.13	20.21	19.92
La ₂ O ₃	7.59	6.18	8.15	9.59	7.61	7.48	7.47	7.48	6.83	5.65	5.72	6.20	6.04	6.40	9.58	8.09
Ce ₂ O ₃	10.09	7.62	10.02	9.97	9.91	10.20	10.23	10.24	10.52	9.04	7.76	9.69	10.11	9.41	9.94	8.99
Pr ₂ O ₃	0.61	0.61	0.62	0.56	0.74	0.56	0.75	0.64	0.75	0.73	0.74	0.74	0.74	0.70	0.88	0.71
Nd ₂ O ₃	1.40	1.38	1.39	1.29	1.90	1.23	2.12	1.61	2.36	2.30	2.20	2.20	2.00	1.98	2.88	1.87
ThO ₂	0.16	0.18	0.03	0.43	0.11	0.15	0.10	0.02	0.01	0.01	0.00	0.13	0.05	0.10	0.00	0.05
F	0.38	0.00	0.16	0.11	0.13	0.05	0.12	0.28	0.15	0.10	0.00	0.14	0.14	0.13	0.12	0.20
Total	97.38	97.45	97.45	98.22	95.62	96.64	98.08	93.67	95.96	94.50	96.73	95.12	96.63	96.68	95.39	95.09
Formula Calculation Based on 8 Cations and 12.5 Oxygens																
Mg	0.09	0.09	0.10	0.06	0.09	0.08	0.06	0.13	0.12	0.13	0.11	0.13	0.12	0.11	0.12	0.12
Al	1.22	1.39	1.37	1.13	1.01	1.34	1.14	1.02	0.92	1.17	1.33	1.00	0.99	1.11	0.99	1.15
Si	2.94	2.99	2.95	2.95	2.94	2.96	2.95	2.99	2.97	3.03	3.00	2.97	2.96	2.95	3.05	3.01
Ca	1.31	1.49	1.32	1.31	1.26	1.35	1.31	1.24	1.23	1.37	1.51	1.24	1.27	1.33	1.21	1.31
Ti	0.05	0.04	0.04	0.04	0.04	0.02	0.05	0.05	0.06	0.07	0.04	0.06	0.06	0.05	0.05	0.03
Mn	0.01	0.01	0.01	0.01	0.02	0.01	0.02	0.01	0.02	0.02	0.02	0.02	0.02	0.02	0.02	0.02
Fe ²⁺	0.60	0.48	0.62	0.69	0.68	0.63	0.66	0.64	0.67	0.53	0.48	0.63	0.62	0.59	0.71	0.60
Fe ³⁺	0.98	0.98	0.84	1.02	1.20	0.91	1.06	1.11	1.24	1.03	0.96	1.24	1.26	1.16	0.97	1.00
La	0.26	0.21	0.28	0.34	0.27	0.26	0.26	0.27	0.25	0.20	0.19	0.22	0.21	0.22	0.35	0.29
Ce	0.34	0.25	0.34	0.35	0.35	0.35	0.35	0.37	0.38	0.32	0.26	0.34	0.35	0.33	0.36	0.32
Pr	0.02	0.02	0.02	0.02	0.03	0.02	0.03	0.02	0.03	0.03	0.02	0.03	0.03	0.02	0.03	0.02
Nd	0.05	0.04	0.05	0.04	0.07	0.04	0.07	0.06	0.08	0.08	0.07	0.08	0.07	0.07	0.10	0.06
Th	0.00	0.00	0.00	0.01	0.00	0.00	0.00	0.00	0.00	0.00	0.00	0.00	0.00	0.00	0.00	0.00
F	0.11	0.00	0.05	0.03	0.04	0.02	0.04	0.09	0.05	0.03	0.00	0.04	0.04	0.04	0.04	0.06
Total	8.00	8.00	8.00	8.00	8.00	8.00	8.00	8.00	8.00	8.00	8.00	8.00	8.00	8.00	8.00	8.00
Fe ³⁺ / (Fe ²⁺ + Fe ³⁺)	0.62	0.67	0.57	0.60	0.64	0.59	0.62	0.63	0.65	0.66	0.67	0.66	0.67	0.66	0.58	0.63

Appendix B

Table A2. Trace element analysis result (ppm) of the Beiya and Machangqing allanite by laser ablation-inductively coupled plasma-mass spectrometry (LA-ICP-MS).

Point	Y	La	Ce	Pr	Nd	Sm	Eu	Gd	Tb	Dy	Ho	Er	Tm	Yb	Lu	Pb	Th	U	ΣREE ¹	LREE/HREE ²	δEu ³
Beiya																					
W364-1-1-1	112	88,190	78,250	4031	7932	434	39.8	387	22.4	26.1	2.32	5.55	0.60	2.87	0.58	58.8	5584	106	179,324	399	0.29
W364-1-1-2	197	87,032	76,961	3962	7674	467	42.8	394	25.1	40.2	4.36	9.71	0.95	4.86	0.98	30.3	2065	112	176,619	367	0.30
W364-1-1-3	246	90,744	81,062	4239	8510	545	49.3	429	28.3	49.1	5.01	11.6	1.13	5.59	1.18	34.2	3694	121	185,680	349	0.30
W364-1-1-4	70	85,047	77,369	3975	7783	365	35.6	368	20.0	17.5	1.67	3.30	0.25	1.99	0.28	54.0	5638	77.7	174,988	423	0.29
W364-1-1-5	378	71,321	64,075	3312	6620	417	41.6	329	23.0	50.9	6.78	22.3	2.73	15.6	3.36	43.0	4264	109	146,241	321	0.33
W364-1-2-1	60	86,728	74,131	3860	7937	389	32.0	432	23.4	19.6	1.87	4.30	0.32	2.40	0.54	18.9	1283	140	173,562	357	0.24
W364-1-2-2	152	90,608	75,867	3829	7818	430	40.6	449	27.3	34.4	3.76	8.90	0.80	5.28	0.78	30.5	2697	210	179,121	337	0.28
W364-1-2-3	1125	91,277	74,072	3876	8579	696	78.9	521	48.2	149	24.2	78.3	11.1	77.4	16.0	54.6	3922	591	179,504	193	0.38
W364-1-2-4	888	93,501	72,101	3602	7521	559	56.5	476	41.5	129	19.7	64.6	9.13	59.0	12.6	65.5	7621	514	178,151	219	0.33
W364-1-2-5	274	90,340	79,374	3991	8041	461	43.4	465	30.3	49.6	5.70	14.4	1.54	8.69	1.71	57.8	6262	100	182,827	316	0.28
W364-1-2-6	153	86,134	77,174	4050	8276	394	38.4	433	25.8	31.6	3.52	8.40	0.70	4.76	0.79	46.9	6182	160	176,575	346	0.28
W364-1-3-1	88	91,428	80,502	4061	8084	456	43.6	390	22.0	24.8	2.03	4.22	0.41	1.94	0.27	76.6	5855	101	185,020	414	0.31
W364-1-3-2	184	85,556	74,594	3827	7759	524	49.9	378	24.0	36.7	3.99	8.05	1.05	5.62	0.97	60.5	5744	174	172,768	376	0.33
W364-1-3-3	342	61,450	53,671	2748	5644	363	39.0	280	19.9	46.6	7.24	21.0	2.82	16.9	3.60	41.8	3123	139	124,313	311	0.36
W364-1-3-4	307	76,803	67,700	3595	7472	510	49.8	361	24.8	53.5	6.32	16.4	1.82	9.87	1.86	25.6	868	117	156,606	328	0.34
W364-1-4-1	315	83,411	74,454	3915	7774	522	48.0	403	27.4	51.2	6.30	16.9	2.18	11.0	2.35	69.0	3938	131	170,641	327	0.31
W364-1-4-2	239	84,105	76,770	4035	8153	556	51.0	410	26.9	43.8	4.94	11.8	1.21	6.89	1.38	54.4	3564	126	174,176	342	0.31
W364-1-4-3	239	82,493	74,052	3814	7593	476	45.4	391	25.1	43.4	5.09	12.4	1.46	7.29	1.62	49.7	4091	147	168,960	346	0.31
W364-1-5-1	309	93,552	81,005	4310	9329	545	53.7	469	31.5	57.6	7.00	18.1	2.30	14.7	2.65	39.6	4224	156	189,398	313	0.32
W364-1-5-2	344	84,817	73,759	3885	8303	498	50.6	423	29.6	57.9	7.43	21.2	2.57	15.4	2.89	40.2	3189	144	171,872	306	0.33
W364-1-5-4	1417	70,755	63,304	3435	7741	566	66.2	409	43.0	172	31.3	103	13.3	75.2	11.7	85.5	2842	220	146,724	170	0.40
W364-1-6-1	449	91,263	77,900	3998	8317	523	57.1	437	31.9	68.6	9.40	27.2	3.11	19.8	4.03	38.7	2678	273	182,660	303	0.36
W364-1-6-2	744	94,880	84,790	4660	10,633	815	75.2	530	45.5	126	17.8	51.1	6.27	37.0	6.75	34.6	3772	137	196,673	239	0.33
W364-1-6-3	250	93,433	82,559	4389	9236	485	44.8	441	28.1	47.7	5.80	15.7	1.84	11.0	2.24	39.6	4871	142	190,701	343	0.29
W364-1-7-1	392	75,673	68,766	3703	7764	535	51.4	373	26.6	57.6	7.62	21.4	2.44	12.5	2.70	32.6	2251	165	156,997	310	0.33
W364-1-7-2	204	73,150	65,767	3477	7100	482	49.2	341	23.0	40.1	4.60	11.0	1.01	6.54	1.30	39.3	1615	178	150,455	350	0.35
W364-1-7-3	347	75,715	67,630	3562	7495	525	52.8	355	25.6	55.1	7.42	21.6	2.49	14.7	3.40	49.2	4527	244	155,466	319	0.35
W364-1-7-6	322	77,918	69,538	3710	7768	537	50.5	375	26.0	56.3	6.24	17.0	1.99	11.1	2.06	43.4	2484	171	160,018	322	0.33
W364-1-7-7	355	81,574	71,970	3782	7904	565	60.5	387	28.1	60.8	7.73	21.2	2.41	14.1	3.29	43.9	3046	265	166,380	316	0.37
W364-2-1-1	116	83,510	71,715	3833	7621	503	55.0	350	14.8	33.7	3.76	6.84	0.73	4.56	0.82	16.7	3941	126	167,649	403	0.38
W364-2-1-2	161	88,204	77,854	4300	8725	589	51.6	410	18.7	41.5	4.97	10.4	1.14	7.17	1.23	13.3	1901	112	180,219	363	0.30
W364-2-1-3	125	72,795	61,568	2939	6459	413	43.3	299	13.1	29.6	3.75	8.82	1.19	8.78	1.30	13.3	2906	95.8	144,583	394	0.36
W364-2-2-2	227	76,480	69,984	3913	8344	616	62.6	421	22.7	60.2	7.22	13.1	1.60	10.6	1.91	11.4	2288	221	159,937	296	0.36
W364-2-3-2	240	89,916	78,004	4189	8310	552	60.0	404	21.1	57.9	8.90	20.3	2.95	21.7	3.78	16.9	4110	207	181,571	335	0.37
W364-2-4-1	244	86,993	76,427	4184	8527	601	63.6	418	21.6	57.1	8.40	20.1	2.69	18.7	3.24	21.3	3706	166	177,345	322	0.37
W364-2-4-2	106	87,600	77,718	4246	8551	547	53.5	369	14.4	28.6	3.32	6.70	0.81	5.30	0.84	16.9	4022	100	179,145	416	0.34
W364-2-7-1	471	87,816	74,173	3883	7816	552	62.5	415	26.4	92.3	16.2	42.4	5.79	44.6	7.66	11.5	1667	158	174,953	268	0.38
W364-2-7-2	105	83,101	71,510	3651	7135	415	44.6	320	13.7	29.6	3.65	8.06	1.06	5.95	1.06	14.1	2994	162	166,240	433	0.36
W364-2-12-1	116	92,496	77,834	3923	8247	507	51.2	356	14.3	28.9	2.91	7.33	1.23	6.93	0.97	22.1	5393	101	183,478	437	0.35

Table A2. Cont.

Point	Y	La	Ce	Pr	Nd	Sm	Eu	Gd	Tb	Dy	Ho	Er	Tm	Yb	Lu	Pb	Th	U	ΣREE ¹	LREE/HREE ²	δEu ³
Machangqing																					
JDS03-01-01	107	62,099	73,116	5212	11,996	505	35.8	154	10.7	27.6	3.49	7.19	0.85	3.78	0.34	18.2	2107	142	153,172	735	0.30
JDS03-01-02	168	58,984	74,123	5619	14,018	730	82.6	214	15.6	43.4	5.85	11.4	1.21	4.48	0.64	14.9	1255	145	153,854	517	0.49
JDS03-01-03	158	53,984	67,027	5469	14,304	774	90.8	208	14.5	44.4	5.95	11.3	1.14	6.84	0.85	11.8	1072	54.4	141,942	484	0.52
JDS03-01-04	98.5	59,859	72,724	5206	11,784	515	45.7	152	10.4	27.4	3.44	6.88	0.69	2.88	0.30	23.5	1027	114	150,337	737	0.38
JDS03-01-05	126	57,194	71,090	5483	13,862	668	78.6	166	11.8	34.5	4.91	9.20	0.88	4.98	0.53	13.9	1260	54.4	148,608	637	0.52
JDS03-01-06	141	63,207	74,775	5313	11,943	566	56.2	178	13.6	38.5	5.48	9.91	0.90	4.13	0.43	21.8	1183	118	156,112	621	0.42
JDS03-01-07	130	53,825	66,743	5092	12,867	789	99.3	214	15.4	42.3	5.13	9.14	0.91	5.48	0.82	11.5	1381	117	139,708	476	0.55
JDS03-01-08	179	60,330	68,892	4776	11,043	627	71.1	187	15.4	46.8	6.65	13.3	1.31	6.52	0.80	11.9	1519	108	146,016	525	0.49
JDS03-01-09	172	54,724	63,927	4614	10,898	612	51.3	191	15.0	45.9	5.98	11.8	1.12	5.22	0.50	14.5	1505	121	135,103	488	0.36
JDS03-01-10	42.2	53,263	64,195	4932	11,759	508	49.1	107	6.21	13.2	1.69	3.04	0.23	2.17	0.31	10.0	582	30.1	134,840	1005	0.44
JDS03-01-11	255	62,816	79,496	6306	16,284	1040	111	269	23.4	70.2	9.49	20.7	2.20	11.3	1.42	8.24	847	54.1	166,460	407	0.47
JDS03-01-12	37.2	60,528	68,162	4827	10,524	403	42.8	104	5.57	13.6	1.37	2.70	0.27	0.96	0.17	7.87	406	39.5	144,614	1127	0.47
JDS03-01-13	35.2	59,013	72,146	5297	11,863	429	41.7	96.1	4.71	10.7	1.42	2.77	0.24	1.52	0.27	28.7	465	23.5	148,909	1263	0.44
JDS03-01-15	192	58,306	74,330	5875	14,833	881	106	225	18.4	55.6	7.36	13.9	1.44	8.01	0.92	12.3	714	54.5	154,662	467	0.53
JDS03-01-21	41.8	61,777	73,417	5049	10,791	391	35.4	94.7	5.62	12.7	1.68	2.89	0.23	1.50	0.18	7.55	613	37.1	151,580	1267	0.40
JDS03-01-23	206	58,679	72,480	5706	14,364	795	82.4	203	17.1	54.4	7.50	15.2	1.79	8.49	0.99	12.4	763	52.7	152,415	493	0.46
JDS03-01-24	70.6	57,302	68,367	4967	11,583	470	47.2	116	8.26	22.0	2.59	5.98	0.52	3.03	0.43	16.5	606	49.4	142,894	899	0.45
JDS03-01-25	41.6	62,297	72,666	5141	11,029	324	33.3	81.1	4.95	12.6	1.49	3.31	0.35	1.30	0.19	7.68	560	26.5	151,597	1439	0.46
JDS03-01-27	532	60,070	77,383	6404	18,150	1442	166	422	42.8	138	19.8	40.7	4.48	23.5	2.67	7.22	906	89.1	164,308	236	0.50
JDS03-01-28	451	60,173	78,770	6682	19,085	1393	128	387	37.7	125	16.7	34.3	3.95	16.7	2.24	6.36	859	80.0	166,854	267	0.40
JDS03-01-29	327	59,457	76,180	6194	16,993	1124	130	308	28.7	90.5	11.8	24.4	2.62	13.0	1.64	6.96	832	71.2	160,560	333	0.51
JDS03-01-30	148	60,324	72,523	5317	13,111	638	82.8	165	13.0	39.6	5.28	10.7	1.06	6.45	0.82	7.58	739	72.9	152,238	628	0.57
JDS03-01-31	307	62,877	74,996	5501	14,073	885	108	262	24.2	80.3	11.2	23.4	2.54	13.3	1.66	8.84	825	86.9	158,859	378	0.53
JDS03-01-32	244	60,304	73,398	5487	13,750	814	93.8	224	20.2	64.9	8.53	17.3	1.83	7.64	1.01	8.33	747	102	154,193	446	0.50
JDS03-01-33	248	59,246	73,606	5699	14,554	875	88.9	232	21.1	68.5	9.33	18.2	1.85	9.76	1.24	14.3	637	72.3	154,431	426	0.45
JDS03-01-34	321	42,699	54,658	4467	12,219	873	112	248	24.2	83.8	11.0	23.4	2.58	14.3	1.57	8.03	547	89.6	115,437	282	0.56
JDS03-01-37	251	56,208	67,943	5361	13,328	831	109	231	20.3	67.9	9.15	18.4	1.83	8.97	1.22	9.04	723	102	144,140	401	0.57

¹ ΣREE means total rare earth element; ² LREE (light rare earth element) = La + Ce + Pr + Nd + Sm + Eu; HREE (heavy rare earth element) = Gd + Tb + Dy + Ho + Er + Tm + Yb + Lu;

³ δEu = (Eu/Eu*)_N = Eu_N/((1/2)Sm_N + (1/2)Gd_N).

Appendix C

Table A3. LA-ICP-MS U-Th-Pb isotope data for allanite from the Beiy and Machangqing deposits.

Point	Measured Value								²⁰⁷ Pb Correction			
	Th/U	²⁰⁷ Pb/ ²⁰⁶ Pb		²⁰⁷ Pb/ ²³⁵ U		²⁰⁶ Pb/ ²³⁸ U		²⁰⁸ Pb/ ²³² Th		<i>f</i> ²⁰⁶	²³² Th _m / ²⁰⁶ Pb _c	²⁰⁸ Pb _m / ²⁰⁶ Pb _c
		Ratio	1sigma	Ratio	1sigma	Ratio	1sigma	Ratio	1sigma			
Beiya												
W364-1-1-1	52.4	0.7431	0.0215	4.4970	0.1902	0.0439	0.0016	0.0032	0.0001	0.85	1788	5.8
W364-1-1-2	18.4	0.6715	0.0243	2.6101	0.0924	0.0282	0.0008	0.0043	0.0001	0.76	1052	4.6
W364-1-1-3	30.5	0.6563	0.0303	2.0378	0.0821	0.0225	0.0005	0.0029	0.0000	0.75	2319	6.7
W364-1-1-4	72.5	0.7589	0.0307	5.2115	0.1907	0.0498	0.0015	0.0030	0.0000	0.87	2129	6.4
W364-1-1-5	39.2	0.7262	0.0246	3.2016	0.0950	0.0320	0.0009	0.0031	0.0001	0.83	1855	5.8
W364-1-2-1	9.2	0.6107	0.0292	1.4945	0.0556	0.0177	0.0005	0.0046	0.0001	0.69	946	4.4
W364-1-2-2	12.8	0.5440	0.0232	1.2708	0.0463	0.0169	0.0004	0.0037	0.0001	0.61	1557	5.7
W364-1-2-3	6.6	0.5277	0.0172	0.9780	0.0317	0.0134	0.0002	0.0043	0.0001	0.59	1072	4.6
W364-1-2-4	14.8	0.4751	0.0185	0.8848	0.0287	0.0135	0.0003	0.0028	0.0001	0.52	2687	7.6
W364-1-2-5	62.8	0.7554	0.0290	4.9157	0.2147	0.0472	0.0017	0.0030	0.0001	0.87	1990	6.0
W364-1-2-6	38.6	0.6497	0.0295	1.7593	0.0796	0.0196	0.0006	0.0025	0.0001	0.74	3466	8.8
W364-1-3-1	57.8	0.7611	0.0293	6.8840	0.3134	0.0656	0.0021	0.0037	0.0001	0.87	1289	4.8
W364-1-3-2	33.0	0.7147	0.0295	2.7180	0.1356	0.0276	0.0009	0.0032	0.0001	0.82	1866	6.0
W364-1-3-3	22.4	0.6777	0.0311	2.7394	0.1124	0.0293	0.0008	0.0040	0.0001	0.77	1233	5.0
W364-1-3-4	7.4	0.6689	0.0369	2.4998	0.1344	0.0271	0.0011	0.0080	0.0003	0.76	450	3.6
W364-1-4-1	30.0	0.7466	0.0278	5.2608	0.1728	0.0511	0.0012	0.0050	0.0001	0.86	870	4.3
W364-1-4-2	28.3	0.7603	0.0241	4.5014	0.1703	0.0429	0.0013	0.0044	0.0001	0.87	964	4.3
W364-1-4-3	27.8	0.6389	0.0238	2.8627	0.0860	0.0325	0.0007	0.0037	0.0001	0.72	1508	5.5
W364-1-5-1	27.1	0.6280	0.0302	2.0604	0.0826	0.0238	0.0008	0.0030	0.0001	0.71	2046	6.1
W364-1-5-2	22.2	0.6842	0.0284	2.6896	0.1098	0.0285	0.0009	0.0039	0.0001	0.78	1298	5.0
W364-1-5-4	12.9	0.6390	0.0227	2.1352	0.0846	0.0242	0.0007	0.0046	0.0001	0.72	866	3.9
W364-1-6-1	9.8	0.5325	0.0224	1.3792	0.0513	0.0188	0.0005	0.0044	0.0001	0.59	1126	4.9
W364-1-6-2	27.6	0.6289	0.0300	1.9941	0.0802	0.0230	0.0007	0.0030	0.0001	0.71	2181	6.6
W364-1-6-3	34.3	0.6041	0.0275	1.9778	0.0823	0.0237	0.0006	0.0027	0.0001	0.68	2715	7.3
W364-1-7-1	13.7	0.6579	0.0405	2.0285	0.0613	0.0224	0.0007	0.0043	0.0001	0.75	1033	4.4
W364-1-7-2	9.1	0.7118	0.0272	2.6038	0.1056	0.0265	0.0009	0.0069	0.0002	0.81	528	3.6
W364-1-7-3	18.6	0.6393	0.0316	1.7007	0.0600	0.0193	0.0007	0.0033	0.0001	0.73	1671	5.5
W364-1-7-6	14.5	0.6982	0.0290	2.5858	0.0963	0.0269	0.0006	0.0050	0.0001	0.80	841	4.2
W364-1-7-7	11.5	0.5876	0.0323	1.4915	0.0642	0.0184	0.0005	0.0040	0.0001	0.66	1203	4.9

Table A3. Cont.

Point	Measured Value										²⁰⁷ Pb Correction		
	Th/U	²⁰⁷ Pb/ ²⁰⁶ Pb		²⁰⁷ Pb/ ²³⁵ U		²⁰⁶ Pb/ ²³⁸ U		²⁰⁸ Pb/ ²³² Th		<i>f</i> ²⁰⁶	²³² Th _m / ²⁰⁶ Pb _c	²⁰⁸ Pb _m / ²⁰⁶ Pb _c	
		Ratio	1sigma	Ratio	1sigma	Ratio	1sigma	Ratio	1sigma				
Beiya													
W364-2-1-1	31.4	0.6137	0.0451	2.1871	0.1187	0.0258	0.0010	0.0028	0.0001	0.69	2158	6.1	
W364-2-1-2	17.0	0.6762	0.0521	2.4868	0.1418	0.0267	0.0012	0.0044	0.0002	0.77	991	4.3	
W364-2-1-3	30.3	0.6261	0.0485	2.3814	0.1233	0.0276	0.0011	0.0031	0.0001	0.71	1778	5.5	
W364-2-2-2	10.4	0.4296	0.0424	0.8075	0.0450	0.0136	0.0005	0.0031	0.0001	0.47	1742	5.3	
W364-2-3-2	19.9	0.5501	0.0513	1.3131	0.0786	0.0173	0.0007	0.0028	0.0001	0.62	1932	5.4	
W364-2-4-1	22.3	0.5933	0.0325	2.3791	0.1206	0.0291	0.0011	0.0037	0.0001	0.67	1186	4.4	
W364-2-4-2	40.1	0.6376	0.0389	2.7007	0.1291	0.0307	0.0012	0.0030	0.0001	0.72	1868	5.6	
W364-2-7-1	10.6	0.5551	0.0405	1.3432	0.0771	0.0176	0.0007	0.0044	0.0002	0.62	1007	4.5	
W364-2-7-2	18.4	0.5863	0.0372	1.4736	0.0815	0.0182	0.0006	0.0031	0.0001	0.66	1622	5.1	
W364-2-12-1	53.4	0.6725	0.0468	3.6073	0.1912	0.0389	0.0015	0.0029	0.0001	0.77	1912	5.5	
Machangqing													
JDS03-01-01	14.8	0.6794	0.0435	2.5978	0.1797	0.0277	0.0017	0.0049	0.0002	0.81	637	3.1	
JDS03-01-02	8.7	0.6517	0.0409	2.2412	0.1120	0.0249	0.0010	0.0063	0.0002	0.78	429	2.7	
JDS03-01-03	19.7	0.7366	0.0517	4.9660	0.2615	0.0489	0.0024	0.0059	0.0002	0.89	437	2.6	
JDS03-01-04	9.0	0.7316	0.0300	4.8846	0.2934	0.0484	0.0023	0.0121	0.0006	0.88	200	2.4	
JDS03-01-05	23.1	0.7242	0.0383	6.0529	0.3078	0.0606	0.0025	0.0063	0.0002	0.87	430	2.7	
JDS03-01-06	10.0	0.7355	0.0355	4.5322	0.2960	0.0447	0.0025	0.0094	0.0004	0.88	241	2.3	
JDS03-01-07	11.8	0.5890	0.0361	1.8097	0.1118	0.0223	0.0008	0.0047	0.0002	0.70	731	3.5	
JDS03-01-08	14.1	0.6430	0.0343	2.2538	0.1119	0.0254	0.0009	0.0049	0.0002	0.77	644	3.2	
JDS03-01-09	12.4	0.6451	0.0393	2.3189	0.1622	0.0261	0.0014	0.0054	0.0003	0.77	604	3.3	
JDS03-01-10	19.4	0.7950	0.0513	7.8032	0.5084	0.0712	0.0039	0.0101	0.0006	0.96	258	2.6	
JDS03-01-11	15.7	0.7014	0.0875	3.8173	0.2505	0.0395	0.0022	0.0055	0.0002	0.84	475	2.6	
JDS03-01-12	10.3	0.7598	0.1126	5.3281	0.3943	0.0509	0.0034	0.0104	0.0005	0.92	213	2.2	
JDS03-01-13	19.8	0.7851	0.0346	30.0247	1.7873	0.2774	0.0149	0.0300	0.0014	0.95	70	2.1	
JDS03-01-15	13.1	0.7624	0.0344	5.4323	0.2286	0.0517	0.0017	0.0091	0.0003	0.92	266	2.4	
JDS03-01-21	16.5	0.7243	0.0607	4.6693	0.2559	0.0468	0.0021	0.0063	0.0002	0.87	402	2.6	
JDS03-01-23	14.5	0.8001	0.0529	5.9012	0.3253	0.0535	0.0029	0.0093	0.0006	0.97	264	2.4	
JDS03-01-24	12.3	0.7208	0.0328	8.2259	0.5142	0.0828	0.0042	0.0139	0.0008	0.87	166	2.3	
JDS03-01-25	21.2	0.7306	0.0548	6.8960	0.3877	0.0685	0.0037	0.0075	0.0003	0.88	320	2.4	
JDS03-01-27	10.2	0.6055	0.0708	1.5633	0.0763	0.0187	0.0008	0.0045	0.0001	0.72	734	3.3	
JDS03-01-28	10.7	0.6189	0.0610	1.5807	0.0933	0.0185	0.0008	0.0041	0.0001	0.73	772	3.2	
JDS03-01-29	11.7	0.6254	0.0634	2.0887	0.1292	0.0242	0.0011	0.0045	0.0001	0.74	641	2.9	

Table A3. Cont.

Point	Measured Value								²⁰⁷ Pb Correction			
	Th/U	²⁰⁷ Pb/ ²⁰⁶ Pb		²⁰⁷ Pb/ ²³⁵ U		²⁰⁶ Pb/ ²³⁸ U		²⁰⁸ Pb/ ²³² Th		<i>f</i> 206	²³² Th _m / ²⁰⁶ Pb _c	²⁰⁸ Pb _m / ²⁰⁶ Pb _c
		Ratio	1sigma	Ratio	1sigma	Ratio	1sigma	Ratio	1sigma			
JDS03-01-30	10.1	0.7000	0.0472	2.3727	0.1200	0.0246	0.0009	0.0054	0.0002	0.84	486	2.6
JDS03-01-31	9.5	0.6785	0.0565	2.2885	0.1120	0.0245	0.0008	0.0057	0.0002	0.81	463	2.6
JDS03-01-32	7.4	0.6309	0.0435	1.7893	0.0918	0.0206	0.0008	0.0057	0.0002	0.75	472	2.7
JDS03-01-33	8.8	0.7459	0.0366	5.0596	0.4480	0.0492	0.0038	0.0111	0.0009	0.90	197	2.2
JDS03-01-34	6.1	0.6548	0.0456	2.2208	0.1114	0.0246	0.0010	0.0079	0.0003	0.78	307	2.4
JDS03-01-37	7.1	0.6593	0.0466	2.1331	0.1032	0.0235	0.0009	0.0065	0.0002	0.79	374	2.4

References

1. Cox, R.A.; Wilton, D.H.C.; Kosler, J. Laser-ablation U-Th-Pb in situ dating of zircon and allanite: An example from the October Harbour granite, Central Coastal Labrador, Canada. *Can. Mineral.* **2003**, *41*, 273–291. [[CrossRef](#)]
2. Cenki-tok, B.; Oliot, E.; Rubatto, D.; Berger, A.; Engi, M.; Janots, E.; Thomsen, T.B.; Manzotti, P.; Regis, D.; Spandler, C.; et al. Preservation of Permian allanite within an Alpine eclogite facies shear zone at Mt Mucrone, Italy: Mechanical and chemical behavior of allanite during mylonitization. *Lithos* **2011**, *125*, 40–50. [[CrossRef](#)]
3. Janots, E.; Negro, F.; Brunet, F.; Goffé, B.; Engi, M.; Bouybaouène, M.L. Evolution of the REE mineralogy in HP-LT metapelites of the Sebti complex, Rif, Morocco: Monazite stability and geochronology. *Lithos* **2006**, *87*, 214–234. [[CrossRef](#)]
4. Gregory, C.J.; Rubatto, D.; Allen, C.M.; Williams, I.S.; Hermann, J.; Ireland, T. Allanite micro-geochronology: A LA-ICP-MS and SHRIMP U-Th-Pb study. *Chem. Geol.* **2007**, *245*, 162–182. [[CrossRef](#)]
5. Kim, Y.; Cheong, C.-S.; Lee, Y.; Williams, I.S. SHRIMP allanite U-Th-Pb dating of bimodal Triassic metamorphism of Neoproterozoic tonalitic gneisses, Daeijak Island, central Korea. *Geosci. J.* **2009**, *13*, 305–315. [[CrossRef](#)]
6. Jung, S.; Brandt, S.; Nebel, O.; Hellebrand, E.; Seth, B.; Jung, C. The P-T-t paths of high-grade gneisses, Kaoko Belt, Namibia: Constraints from mineral data, U-Pb allanite and monazite and Sm-Nd/Lu-Hf garnet ages and garnet ion probe data. *Gondwana Res.* **2014**, *25*, 775–796. [[CrossRef](#)]
7. Cliff, R.A.; Oberli, F.; Meier, M.; Droop, G.T.R.; Kelly, M. Syn-metamorphic folding in the Tauern Window, Austria dated by Th-Pb ages from individual allanite porphyroblasts. *J. Metamorph. Geol.* **2015**, *33*, 427–435. [[CrossRef](#)]
8. Janots, E.; Engi, M.; Rubatto, D.; Berger, A.; Gregory, C.; Rahn, M. Metamorphic rates in collisional orogeny from in situ allanite and monazite dating. *Geology* **2009**, *37*, 11–14. [[CrossRef](#)]
9. Gregory, C.J.; Rubatto, D.; Hermann, J.; Berger, A.; Engi, M. Allanite behaviour during incipient melting in the southern Central Alps. *Geochim. Cosmochim. Acta* **2012**, *84*, 433–458. [[CrossRef](#)]
10. Rubatto, D.; Regis, D.; Hermann, J.; Boston, K.; Engi, M.; Beltrando, M.; McAlpine, S.R.B. Yo-yo subduction recorded by accessory minerals in the Italian Western Alps. *Nat. Geosci.* **2011**, *4*, 338–342. [[CrossRef](#)]
11. Deng, X.; Li, J.; Wen, G. Dating iron skarn mineralization using hydrothermal allanite-(La) U-Th-Pb isotopes by laser ablation ICP-MS. *Chem. Geol.* **2014**, *382*, 95–110. [[CrossRef](#)]
12. Chen, T.W.; Zhou, M.-F. Ages and compositions of primary and secondary allanite from the Lala Fe-Cu deposit, SW China: Implications for multiple episodes of hydrothermal events. *Contrib. Mineral. Petrol.* **2014**, *168*, 1043. [[CrossRef](#)]
13. Pal, D.C.; Chaudhuri, T.; McFarlane, C.; Mukherjee, A.; Sarangi, A.K. Mineral chemistry and in situ dating of allanite, and geochemistry of its host rocks in the Bagjata uranium mine, Singhbhum Shear Zone, India- Implications for the chemical evolution of REE mineralization and mobilization. *Econ. Geol.* **2011**, *106*, 1155–1171. [[CrossRef](#)]
14. Darling, J.R.; Storey, C.D.; Engi, M. Allanite U-Th-Pb geochronology by laser ablation ICPMS. *Chem. Geol.* **2012**, *292*, 103–115. [[CrossRef](#)]
15. Janots, E.; Rubatto, D. U-Th-Pb dating of collision in the external Alpine domains (Urseren zone, Switzerland) using low temperature allanite and monazite. *Lithos* **2014**, *184*, 155–166. [[CrossRef](#)]
16. Smye, A.J.; Roberts, N.M.W.; Condon, D.J.; Horstwood, M.S.A.; Parrish, R.R. Characterising the U-Th-Pb systematics of allanite by ID and LA-ICPMS: Implications for geochronology. *Geochim. Cosmochim. Acta* **2014**, *135*, 1–28. [[CrossRef](#)]
17. Guo, H.; Xiao, Y.; Xu, L.; Sun, H.; Huang, J.; Hou, Z. Origin of allanite in gneiss and granite in the Dabie orogenic belt, Central East China. *J. Asian Earth Sci.* **2017**, *135*, 243–256. [[CrossRef](#)]
18. McFarlane, C.R.M. Allanite U-Pb geochronology by 193 nm LA ICP-MS using NIST610 glass for external calibration. *Chem. Geol.* **2016**, *438*, 91–102. [[CrossRef](#)]
19. He, Z.H.; Guan, D.R.; He, W.Y.; Zhou, Y.M.; Fu, D.G.; Yang, S.; Wang, L.; Li, W.H.; Su, G.S.; Yang, R. Exploration model of Beiya superlarge gold-polymetallic deposit, northwestern Yunnan. *Miner. Depos.* **2016**, *35*, 261–282.

20. Mao, J.; Zhou, Y.; Liu, H.; Zhang, C.; Fu, D.; Liu, B. Metallogenic setting and ore genetic model for the Beiya porphyry-skarn polymetallic Au orefield, western Yunnan, China. *Ore Geol. Rev.* **2017**, *86*, 21–34. [[CrossRef](#)]
21. Deng, J.; Wang, Q.; Li, G.; Santosh, M. Cenozoic tectono-magmatic and metallogenic processes in the Sanjiang region, southwestern China. *Earth-Sci. Rev.* **2014**, *138*, 268–299. [[CrossRef](#)]
22. Deng, X.D.; Li, J.W.; Zhou, M.F.; Zhao, X.F.; Yan, D.R. In-situ LA-ICPMS trace elements and U-Pb analysis of titanite from the Mesozoic Ruanjiawan W-Cu-Mo skarn deposit, Daye district, China. *Ore Geol. Rev.* **2015**, *65*, 990–1004. [[CrossRef](#)]
23. Hou, Z.; Zeng, P.; Gao, Y.; Du, A.; Fu, D. Himalayan Cu-Mo-Au mineralization in the eastern Indo-Asian collision zone: Constraints from Re-Os dating of molybdenite. *Miner. Depos.* **2006**, *41*, 33–45. [[CrossRef](#)]
24. Fu, Y.; Sun, X.; Lin, H.; Zhou, H.; Li, X.; Ouyang, X.; Jiang, L.; Shi, G.; Liang, Y. Geochronology of the giant Beiya gold-polymetallic deposit in Yunnan Province, Southwest China and its relationship with the petrogenesis of alkaline porphyry. *Ore Geol. Rev.* **2015**, *71*, 138–149. [[CrossRef](#)]
25. Deng, J.; Wang, Q.; Li, G.; Hou, Z.; Jiang, C.; Danyushevsky, L. Geology and genesis of the giant Beiya porphyry-skarn gold deposit, northwestern Yangtze Block, China. *Ore Geol. Rev.* **2015**, *70*, 457–485. [[CrossRef](#)]
26. Liu, B.; Liu, H.; Zhang, C.; Mao, Z.; Zhou, Y.; Huang, H.; He, Z.; Su, G. Geochemistry and geochronology of porphyries from the Beiya gold-polymetallic orefield, western Yunnan, China. *Ore Geol. Rev.* **2015**, *69*, 360–379. [[CrossRef](#)]
27. Fu, Y.; Sun, X.; Zhou, H.; Lin, H.; Jiang, L.; Yang, T. In-situ LA-ICP-MS trace elements analysis of scheelites from the giant Beiya gold-polymetallic deposit in Yunnan Province, Southwest China and its metallogenic implications. *Ore Geol. Rev.* **2017**, *80*, 828–837. [[CrossRef](#)]
28. He, W.; Mo, X.; He, Z.; White, N.C.; Chen, J.; Yang, K.; Wang, R.; Yu, X.; Dong, G.; Huang, F. The geology and mineralogy of the Beiya skarn gold deposit in Yunnan, Southwest China. *Econ. Geol.* **2015**, *110*, 1625–1641. [[CrossRef](#)]
29. Meinert, L.; Hedenquist, J.; Satoh, H.; Matsuhisa, Y. Formation of Anhydrous and Hydrous Skarn in Cu-Au Ore Deposits by Magmatic Fluids. *Econ. Geol.* **2003**, *98*, 147–156. [[CrossRef](#)]
30. Lu, Y.; Kerrich, R.; Kemp, A.I.S.; McCuaig, T.C.; Hou, Z.; Hart, C.J.R.; Li, Z.; Cawood, P.A.; Bagas, L.; Yang, Z.; et al. Intracontinental eocene-oligocene porphyry Cu mineral systems of Yunnan, Western Yangtze Craton, China: Compositional characteristics, sources, and implications for continental collision metallogeny. *Econ. Geol.* **2013**, *108*, 1541–1576. [[CrossRef](#)]
31. Hu, R.; Burnard, P.G.; Turner, G.; Bi, X. Helium and Argon isotope systematics in fluid inclusions of Machangqing copper deposit in west Yunnan Province, China. *Chem. Geol.* **1998**, *146*, 55–63. [[CrossRef](#)]
32. Wang, Z.; Ge, L.; Guo, X.; Wang, L.; Yuan, S.; Yang, L. Epithermal-porphyry Cu-Mo-Au polymetal metallogenic system in Machangqing ore field, Yunnan. *Acta Petrol. Sin.* **2012**, *28*, 1425–1437.
33. Xing, J.; Guo, X.; Qu, W.; Wang, Z.; Li, H. Molybdenite Re-Os age and other geological meaning of Machangqing porphyry copper, molybdenum deposit. *Gold Sci. Technol.* **2009**, *17*, 24–29.
34. Chu, Y.; Liu, X.; Zhao, F.; Lu, Q.; Li, C.; Xiao, J.; Wu, R.; Song, X.; Cai, Y.; Cai, F. Dating of ore-bearing porphyritic granite from the Machangqing Mo-Cu-Au deposit in Western Yunnan Province and its geologic significance. *J. Jilin Univ. Earth Sci. Ed.* **2013**, *43*, 1377–1392.
35. He, W.; Mo, X.; Yu, X.; Li, Y.; Huang, X.; He, Z. Geochronological study of magmatic intrusions and mineralization of Machangqing porphyry Cu-Mo-Au deposit, Western Yunnan Province. *Earth Sci. Front.* **2011**, *18*, 207–215.
36. Guo, X.; Wang, Z.; Wang, L.; Yang, Y.; Che, X. LA-ICP-MS zircon U-Pb ages of granite in Machangqing complex of Yunnan Province and their geological significance. *Geol. China* **2011**, *38*, 610–622. (in Chinese).
37. Chiaradia, M.; Schaltegger, U.; Spikings, R.; Wotzlaw, J.F.; Ovtcharova, M. How accurately can we date the duration of magmatic-hydrothermal events in porphyry systems—An Invited Paper. *Econ. Geol.* **2013**, *108*, 565–584. [[CrossRef](#)]
38. Hou, Z.; Zaw, K.; Pan, G.; Mo, X.; Xu, Q.; Hu, Y.; Li, X. Sanjiang Tethyan metallogenesis in S. W. China: Tectonic setting, metallogenic epochs and deposit types. *Ore Geol. Rev.* **2007**, *31*, 48–87. [[CrossRef](#)]
39. Lai, C.K.; Meffre, S.; Crawford, A.J.; Zaw, K.; Xue, C.D.; Halpin, J.A. The Western Ailaoshan Volcanic Belts and their SE Asia connection: A new tectonic model for the Eastern Indochina Block. *Gondwana Res.* **2014**, *26*, 52–74. [[CrossRef](#)]
40. Lai, C.K.; Meffre, S.; Crawford, A.J.; Zaw, K.; Halpin, J.A.; Xue, C.D.; Salam, A. The central ailaoshan ophiolite and modern analogs. *Gondwana Res.* **2014**, *26*, 75–88. [[CrossRef](#)]

41. Wang, J.; Yin, A.; Harrison, T.M.; Grove, M.; Zhang, Y.; Xie, G. A tectonic model for Cenozoic igneous activities in the eastern Indo-Asian collision zone. *Earth Planet. Sci. Lett.* **2001**, *188*, 123–133. [[CrossRef](#)]
42. Hou, Z.; Zhong, D.; Deng, W. A tectonic model for porphyry copper-molybdenum-gold metallogenic belts on the eastern margin of the Qinghai-Tibet Plateau. *Geol. China* **2004**, *31*, 1–14.
43. Najman, Y.; Appel, E.; Fadel, M.B.; Bown, P.; Carter, A.; Garzanti, E.; Godin, L.; Han, J.; Liebke, U.; Oliver, G.; et al. Timing of India-Asia collision: Geological, biostratigraphic, and palaeomagnetic constraints. *J. Geophys. Res.* **2010**, *115*, 1–18. [[CrossRef](#)]
44. Dupont-Nivet, G.; Lippert, P.C.; Van Hinsbergen, D.J.J.; Meijers, M.J.M.; Kapp, P. Palaeolatitude and age of the Indo-Asia collision: Palaeomagnetic constraints. *Geophys. J. Int.* **2010**, *182*, 1189–1198. [[CrossRef](#)]
45. Chung, S.L.; Chu, M.F.; Zhang, Y.Q.; Xie, Y.W.; Lo, C.H.; Lee, T.Y.; Lan, C.Y.; Li, X.H.; Zhang, Q.; Wang, Y.Z. Tibetan tectonic evolution inferred from spatial and temporal variations in post-collisional magmatism. *Earth Sci. Rev.* **2005**, *68*, 173–196. [[CrossRef](#)]
46. Hou, Z.; Cook, N.J. Metallogenesis of the Tibetan collisional orogen: A review and introduction to the special issue. *Ore Geol. Rev.* **2009**, *36*, 2–24. [[CrossRef](#)]
47. Xu, X.; Cai, X.; Song, B.; Zhang, B.; Ying, H.; Xiao, Q.; Wang, J. Petrologic, chronological and geochemistry characteristics and formation mechanism of alkaline porphyries in the Beiya gold district, western Yunnan. *Acta Petrol. Sin.* **2006**, *22*, 631–642.
48. Xue, C.; Hou, Z.; Liu, X.; Yang, Z.; Liu, Y.; Hao, B. Petrogenesis and metallogenesis of the Beiya gold-polymetallic ore district, northwestern Yunnan province, China: Responses to the Indo-Asian collisional processes. *Acta Petrol. Sin.* **2008**, *24*, 457–472.
49. Xu, X.; Cai, X.; Xiao, Q.; Peters, S.G. Porphyry Cu-Au and associated polymetallic Fe-Cu-Au deposits in the Beiya Area, western Yunnan Province, south China. *Ore Geol. Rev.* **2007**, *31*, 224–246. [[CrossRef](#)]
50. Guo, X.; Wang, Z.; Chen, X.; Wang, X.; Wang, S. Machangqing porphyry Cu-Mo-Au deposit, Yunnan Province: Geological characteristics and its genesis. *Acta Geol. Sin.* **2009**, *83*, 1901–1914.
51. Xu, L.; Bi, X.; Hu, R.; Zhang, X.; Su, W.; Qu, W.; Hu, Z.; Tang, Y. Relationships between porphyry Cu-Mo mineralization in the Jinshajiang-Red River metallogenic belt and tectonic activity: Constraints from zircon U-Pb and molybdenite Re-Os geochronology. *Ore Geol. Rev.* **2012**, *48*, 460–473. [[CrossRef](#)]
52. Liang, H.; Xie, Y.; Zhang, Y.; Campbell, I. Constraints to the mineralization of the copper deposits from forming and evolution of potassium-rich alkali rock at Machangqing copper deposits. *Prog. Nat. Sci.* **2004**, *14*, 116–120.
53. Mao, J.; Pirajno, F.; Lehmann, B.; Luo, M.; Berzina, A. Distribution of porphyry deposits in the Eurasian continent and their corresponding tectonic settings. *J. Asian Earth Sci.* **2014**, *79*, 576–584. [[CrossRef](#)]
54. Li, W.; Wang, J.; He, Z.; Dou, S. Formation of Au-polymetallic ore deposits in alkaline porphyries at Beiya, Yunnan, Southwest China. *Ore Geol. Rev.* **2016**, *73*, 241–252. [[CrossRef](#)]
55. Zhou, H.; Sun, X.; Fu, Y.; Lin, H.; Jiang, L. Mineralogy and mineral chemistry of Bi-minerals: Constraints on ore genesis of the Beiya giant porphyry-skarn gold deposit, southwestern China. *Ore Geol. Rev.* **2016**, *79*, 408–424. [[CrossRef](#)]
56. Lu, Y.; Kerrich, R.; Cawood, P.A.; McCuaig, T.C.; Hart, C.J.R.; Li, Z.; Hou, Z.; Bagas, L. Zircon SHRIMP U-Pb geochronology of potassic felsic intrusions in western Yunnan, SW China: Constraints on the relationship of magmatism to the Jinsha suture. *Gondwana Res.* **2012**, *22*, 737–747. [[CrossRef](#)]
57. Xu, S. *Metallogenic Modeling of the Beiya Gold Deposit in Western Yunnan and Its Relation to the Cenozoic Alkali-Rich Porphyries*; China University of Geosciences: Beijing, China, 2007.
58. He, W.; Mo, X.; Yu, X.; He, Z.; Dong, G.; Liu, X.; Su, G.; Huang, X. Zircon U-Pb and molybdenite Re-Os dating for the Beiya gold-polymetallic deposit in the western Yunnan Province and its geological significance. *Acta Petrol. Sin.* **2013**, *29*, 1301–1310.
59. Jiang, C.; Wang, Q.; Li, G.; Ma, N.; Hu, Z. Relative oxidation states of intrusions in Beiya gold-polymetallic deposit in Sanjiang area, Yunnan, SW China. *Acta Geol. Sin.* **2013**, *29*, 3925–3936.
60. He, W.; Yu, X.; Mo, X.; He, Z.; Li, Y.; Huang, X.; Su, G. Genetic type and the relationship between alkali-rich intrusion and mineralization of Beiya gold-polymetallic ore field, western Yunnan Province, China. *Acta Geol. Sin.* **2012**, *28*, 1401–1421.
61. Fu, Y.; Sun, X.; Zhou, H.; Lin, H.; Yang, T. In-situ LA-ICP-MS U-Pb geochronology and trace elements analysis of polygenetic titanite from the giant Beiya gold-polymetallic deposit in Yunnan Province, Southwest China. *Ore Geol. Rev.* **2016**, *77*, 43–56. [[CrossRef](#)]

62. He, W.Y. *The Beiya Giant Gold-Polymetallic Deposit: Magmatism and Metallogenic Model*; China University of Geosciences: Beijing, China, 2014.
63. Xiao, X.; Yu, X.; Mo, X.; Li, Y.; Huang, X. Geochemical characteristics of the metallogenesis in the gold-polymetallic deposit in Beiya, western Yunnan Province. *Geol. Explor.* **2011**, *47*, 170–179.
64. Guo, X.; Niu, C.; Wang, Z.; Wang, L.; Xia, R. Metallogenic system of Machangqing Cu-Mo-Au polymetallic ore concentration area in Yunnan Province. *Miner. Depos.* **2012**, *31*, 615–628.
65. Wang, D.; Qu, W.; Li, Z.; Yin, H.; Chen, Y. Mineralization episode of porphyry copper deposits in the Jinshajiang-Red River mineralization belt: Re-Os dating. *Sci. China Ser. D* **2005**, *48*, 192–198. [[CrossRef](#)]
66. Pearce, N.J.G.; Perkins, W.T.; Westgate, J.A.; Gorton, M.P.; Jackson, S.E.; Neal, C.R.; Chenery, S.P. A compilation of new and published major and trace element data for NIST SRM 610 and NIST SRM 612 glass reference materials. *Geostand. Newsl.* **1997**, *21*, 115–144. [[CrossRef](#)]
67. Wiedenbeck, M.; Allé, P.; Corfu, F.; Griffin, W.L.; Meier, M.; Oberli, F.; Von Quadt, A.; Roddick, J.C.; Spiegel, W. Three natural zircon standards for U-Th-Pb, Lu-Hf, trace element and REE analyses. *Geostand. Newsl.* **1995**, *19*, 1–23. [[CrossRef](#)]
68. Liu, Y.; Gao, S.; Hu, Z.; Gao, C.; Zong, K.; Wang, D. Continental and oceanic crust recycling-induced melt-peridotite interactions in the Trans-North China Orogen: U-Pb dating, Hf isotopes and trace elements in zircons from mantle xenoliths. *J. Petrol.* **2010**, *51*, 537–571. [[CrossRef](#)]
69. Ludwig, K.R. *User's Manual for Isoplot 3.0: A Geochronological Toolkit for Microsoft Excel*; Berkeley Geochronology Center: Berkeley, CA, USA, 2003.
70. Williams, I. U-Th-Pb geochronology by ion microprobe. *Rev. Econ. Geol.* **1998**, *7*, 1–35.
71. Poitrasson, F. In situ investigations of allanite hydrothermal alteration: Examples from calc-alkaline and anorogenic granites of Corsica (southeast France). *Contrib. Mineral. Petrol.* **2002**, *142*, 485–500. [[CrossRef](#)]
72. Sun, S.S.; McDonough, W.F. Chemical and isotopic systematics of oceanic basalts: Implications for mantle composition and processes. In *Magmatism in the Ocean Basins*; Sander, A.D., Norry, M.J., Eds.; Geological Society Special Publication: London, UK, 1989; Volume 42, pp. 313–345.
73. Schärer, U. The effect of initial ²³⁰Th disequilibrium on young U-Pb ages: The Makalu case, Himalaya. *Earth Planet. Sci. Lett.* **1984**, *67*, 191–204. [[CrossRef](#)]
74. Guo, H.; Xiao, Y.; Gu, X.; Huang, J.; Hou, Z.; Liu, H. LA-ICP-MS allanite U-Th-Pb geochronology study on Guangdong Xinfeng REE-rich granite. *Acta Geol. Sin.* **2014**, *88*, 1025–1037.
75. Zhou, H.; Sun, X.; Cook, N.J.; Lin, H.; Fu, Y.; Zhong, R.; Brugger, J. Nano to micron-scale particulate gold hosted by Magnetite: A product of gold scavenging by bismuth melts. *Econ. Geol.* **2017**, *112*, 993–1010. [[CrossRef](#)]
76. Smith, M.A.P.; Henderson, P.A.U.L.; Jeffries, T.E. The formation and alteration of allanite in skarn from the Beinn a Dubhaich granite aureole, Skye. *Eur. J. Mineral.* **2002**, *14*, 471–486. [[CrossRef](#)]
77. Lancmuir, D.; Herman, J.S. The mobility of thorium in natural waters at low temperatures. *Geochim. Cosmochim. Acta* **1980**, *44*, 1753–1766. [[CrossRef](#)]
78. Sun, W.; Huang, R.; Li, H.; Hu, Y.; Zhang, C.; Sun, S.; Zhang, L.; Ding, X.; Li, C.; Zartman, R.E.; et al. Porphyry deposits and oxidized magmas. *Ore Geol. Rev.* **2015**, *65*, 97–131. [[CrossRef](#)]
79. Einstein, F.; Rao, P.R.; Trotter, J.; Bartlett, N. The crystal structure of gold trifluoride. *J. Chem. Soc. A* **1967**, 478–482. [[CrossRef](#)]

